The Astrophysical Journal, 968:56 (21pp), 2024 June 20 https://doi.org/10.3847/1538-4357/ad4355

An Expanded Set of Los Alamos OPLIB Tables in MESA: Type-1 Rosseland-mean Opacities and Solar Models

Ebraheem Farag[1,2,3], Christopher J. Fontes[2], F. X. Timmes[1], Earl P. Bellinger[3,4,5], Joyce A. Guzik[2], Evan B. Bauer[6], Suzannah R. Wood[2], Katie Mussack[2], Peter Hakel[7], James Colgan[7], David P. Kilcrease[7], Manolo E. Sherrill[7], Tryston C. Raecke[7], and Morgan T. Chidester[1]
[1] School of Earth and Space Exploration, Arizona State University, Tempe, AZ 85287, USA; ekfarag@asu.edu
[2] Center for Theoretical Astrophysics, Los Alamos National Laboratory, Los Alamos, NM 87545, USA
[3] Department of Astronomy, Yale University, New Haven, CT 06511, USA
[4] Max-Planck-Institut für Astrophysik, Karl-Schwarzschild-Straße 1, D-85741 Garching, Germany
[5] Stellar Astrophysics Centre, Aarhus University, Aarhus, Denmark
[6] Center for Astrophysics | Harvard & Smithsonian, 60 Garden Street, Cambridge, MA 02138, USA
[7] Los Alamos National Laboratory, Los Alamos, NM 87545, USA
Received 2023 November 27; revised 2024 April 16; accepted 2024 April 16; published 2024 June 11

Abstract

We present a set of 1194 Type-1 Rosseland-mean opacity tables for four different metallicity mixtures. These new Los Alamos OPLIB atomic radiative opacity tables are an order of magnitude larger in number than any previous opacity table release, and span regimes where previous opacity tables have not existed. For example, the new set of opacity tables expands the metallicity range to $Z = 10^{-6}$ to $Z = 0.2$, which allows improved accuracy of opacities at low and high metallicity, increases the table density in the metallicity range $Z = 10^{-4}$ to $Z = 0.1$ to enhance the accuracy of opacities drawn from interpolations across neighboring metallicities, and adds entries for hydrogen mass fractions between $X = 0$ and $X = 0.1$ including $X = 10^{-2}$, 10^{-3}, 10^{-4}, 10^{-5}, 10^{-6} that can improve stellar models of hydrogen deficient stars. We implement these new OPLIB radiative opacity tables in MESA and find that calibrated solar models agree broadly with previously published helioseismic and solar neutrino results. We find differences between using the new 1194 OPLIB opacity tables and the 126 OPAL opacity tables range from ≈20% to 80% across individual chemical mixtures, up to ≈8% and ≈15% at the bottom and top of the solar convection zone respectively, and ≈7% in the solar core. We also find differences between standard solar models using different opacity table sources that are on par with altering the initial abundance mixture. We conclude that this new, open-access set of OPLIB opacity tables does not solve the solar modeling problem, and suggest the investigation of physical mechanisms other than the atomic radiative opacity.

Unified Astronomy Thesaurus concepts: Stellar atmospheric opacity (1585); Stellar interiors (1606); Stellar physics (1621); Stellar evolution (1599)

1. Introduction

The radiative opacity κ, a cross section per unit mass usually expressed in centimeters squared per gram, describes the absorption and scattering of photons in a medium. It is a crucial component of stellar physics that, in the interior, relates the diffusive transport of the photon-energy flux F_γ to spatial gradients in the energy density of the radiation field: $F_\gamma \propto (1/\kappa)\, d(T^4)/dr$, where T is the temperature and r is the radial distance (Mihalas & Mihalas 1984).

The radiative opacity depends on the energy of the photons and three other quantities shared with the stellar equation of state—the temperature T, density ρ, and composition vector. As a result, κ and its partial derivatives with respect to thermodynamic quantities can impact a wide range of stellar phenomena.

For example, the κ mechanism drives changes in the luminosity of many types of pulsating variable stars (Eddington 1926; Cox 1980; Aerts et al. 2010). In regions where the opacity increases with temperature (e.g., where hydrogen and helium are partly ionized), the atmosphere becomes unstable against pulsations (Hansen et al. 2004; Kippenhahn et al. 2012; Das et al. 2020; Kurtz 2022). Hydrogen ionization drives the pulsations of Mira variables (Fox & Wood 1982; Fadeyev 2022) and red supergiants (Heger et al. 1997; Yoon & Cantiello 2010), the high-overtone, low-degree, nonradial pressure modes of rapidly oscillating Ap stars (Kurtz 1982; Shibahashi & Takata 1993; Bigot & Dziembowski 2002; Holdsworth et al. 2021), and ZZ Ceti variables (Landolt 1968; Córsico et al. 2019). Helium ionization drives pulsations in RR Lyrae variables (Smith 2004; Ngeow et al. 2022) and δ Scuti variables (Balona 2018; Bowman & Kurtz 2018; Guzik 2021; Murphy et al. 2023), DBV white dwarf variables (Córsico et al. 2019; Saumon et al. 2022), and is furthermore responsible for acoustic glitches in solar-like oscillators (Gough 1990; Basu et al. 2004; Mazumdar et al. 2014; Verma et al. 2017, 2019; Saunders et al. 2023). Other opacity increases from the iron group elements (Cr, Fe, Ni, and Cu) at temperatures of $\simeq 2 \times 10^5$ K and densities of $\simeq 10^{-7}$ g cm^{-3} are likely the cause of pulsations in B-type stars (Townsend 2005; Aerts et al. 2010; Guzik et al. 2018; Shi et al. 2023), and β-Cephei variables (e.g., β Centauri, γ Pegasi, and ν Eridani), where κ may account for differences between the observed and calculated pulsation periods (Daszyńska-Daszkiewicz & Walczak 2009, 2010; Cugier 2012; Walczak et al. 2015).

Another example is the solar structure (Basu 2016; Buldgen et al. 2019; Christensen-Dalsgaard 2021), where the ionization

of C, N, O, Ne, and Fe group elements near the base of the solar convection zone induces bound–free transitions that can be a source of the discrepancy between inferences from helioseismology measurements and solar photosphere composition determinations (Neuforge-Verheecke et al. 2001a, 2001b; Turck-Chièze et al. 2004; Bahcall et al. 2006; Basu & Antia 2008; Guzik 2008; Guzik & Mussack 2010; Krief et al. 2016; Pradhan 2024).

The differences between theoretical opacities and observation-adjusted opacities are discussed in Eddington (1926), Daszyńska-Daszkiewicz et al. (2017), Guzik et al. (2018), and Daszyńska-Daszkiewicz et al. (2023). Considerations of negative hydrogen ion transitions (Wildt 1939; Chandrasekhar 1944; Chandrasekhar & Breen 1946; Ohmura & Ohmura 1960; Ohmura 1964; Doughty & Fraser 1966), bound–bound transitions (Mayer 1947; Meyerott & Moszkowski 1951; Moszkowski & Meyerott 1951), bound–free transitions (photoionization), free–free transitions (inverse Bremsstrahlung), and electron scattering (Vitense 1951; Schwarzschild 1958; Vardya 1964; Jin 1982; Meyer-Hofmeister 1982) have been followed by an extensive literature reporting atomic radiative opacity calculations.

Examples include Los Alamos/OPLIB (Cox & Stewart 1962, 1970a, 1970b; Cox 1965; Cox & Tabor 1976; Hübner et al. 1977; Weiss et al. 1990; Magee et al. 1995; Colgan et al. 2016), the Opacity Project (OP; Seaton 1987, 2005; Seaton et al. 1994; Seaton & Badnell 2004; Badnell et al. 2005; Nahar et al. 2024; Pradhan 2024; Pradhan et al. 2024; Zhao et al. 2024), Livermore OPAL (Rogers & Iglesias 1992; Iglesias & Rogers 1993, 1996), analytic fitting (Christy 1966; Stellingwerf 1975a, 1975b; Iben 1975), the Scotland model (Carson et al. 1968; Carson 1976), the OPAS model (Blancard et al. 2012; Le Pennec et al. 2015; Mondet et al. 2015), the hybrid model SCO-RCG (Iglesias & Sonnad 2012; Pain & Gilleron 2015; Pain et al. 2017; Pain & Gilleron 2019) for actinides (Flörs et al. 2023; Fontes et al. 2023), and for He-dominated compositions, He^- free–free (Somerville 1965; John 1994), He_2^+ bound–free and free–free (Ignjatović et al. 2009), He Rayleigh scattering (Iglesias et al. 2002; Rohrmann 2018), and triple-He collisions (Kowalski 2014; Blouin et al. 2019; Saumon et al. 2022).

In this article, we add a novel contribution to this canon by providing open access to an expanded set of 1194 Type-1 Rosseland mean opacity tables for four different heavy element mixtures, with improvements to the composition range, table coverage, and table resolution. Section 2 describes the methods used to construct the opacity tables and highlights a few representative results. Section 3 implements the new opacity tables in `MESA` and applies them to the helioseismology and neutrino fluxes of standard solar models, and Section 4 offers concluding remarks. Appendices A to C detail the implementation and verification of the new Los Alamos opacity tables in `MESA`.

Important symbols are defined in Table 1. In this article "log" refers to the base-10 logarithm; where the natural logarithm is intended, we use "ln."

Table 1
Important Symbols

Name	Description	Appears
α	^{4}He particle	3.3
a	Radiation constant $= 4\sigma/c$	2
A	Atomic number	1
c	Speed of light in the medium	2
c_s	Acoustic sound speed	3.3
G	Gravitational constant	2
E	Energy	2
γ	Photon	3.3
Γ_3	$\equiv d\ln T/d\ln\rho\|_S + 1$	2
h	Planck constant	2
k_B	Boltzmann constant	2
κ	Opacity	1
κ_ν	Monochromatic opacity	2
κ_P	Planck mean opacity	2
κ_R	Rosseland mean opacity	2
λ	Mean free path	2
L	Luminosity	2
M	Stellar mass	2
ν	Frequency	2
ν_e	Electron neutrino	3.3
$\nabla_{\rm rad}$	Radiative temperature gradient	2
r	Radial coordinate	1
R	Opacity coordinate	2
R_o	Stellar radius	2
ρ	Mass density	1
Φ	Neutrino Flux	3.3
P	Pressure	2
σ	Stefan–Boltzmann constant	2
S	Entropy per gram	2
t	Time	2
T	Temperature	1
X	Hydrogen mass fraction	2
Y	Helium mass fraction	2
Z	Metal mass fraction	2
Z	Atomic charge	2

Note. Some symbols may be further subscripted, for example, by an a (indicating an absorption quantity), by an s (indicating a scattering quantity), or by a t (indicating a total quantity).

2. Stellar Opacity

The total monochromatic radiative opacity $\kappa_{\nu,\rm t}$ is the sum of the absorption opacity $\kappa_{\nu,\rm a}$ and scattering opacity $\kappa_{\nu,\rm s}$ at specific T, ρ, and composition. The mean (or gray) opacity represents, in a single number, the tendency of a material to absorb and scatter radiation of all frequencies. Two common mean opacities are the Planck mean (or emission mean) and Rosseland mean opacities. Other examples include a flux-weighted mean and an absorption mean. These various means arise in order to obtain correct values for a particular frequency-integrated physical quantity, such as the radiation flux or energy (Cox & Giuli 1968; Mihalas 1978; Cowan 1981; Mihalas & Mihalas 1984; Hansen et al. 2004; Kippenhahn et al. 2012; Huebner & Barfield 2014; Fontes et al. 2015, 2023).

The Planck mean opacity κ_P yields the correct value for the integrated thermal emission for an optically thin plasma

$$\kappa_P = \frac{\int_0^\infty \kappa_{\nu,\rm a}\, B_\nu(T)\, d\nu}{\int_0^\infty B_\nu(T)\, d\nu}, \tag{1}$$

where $B_\nu(T) = 2h\nu^3/c^2 \cdot 1/(\exp(h\nu/k_BT) - 1)$ is the Planck function, k_B is the Boltzmann constant, h is the Planck constant, c is the medium's speed of light, and ν is the photon frequency. Note κ_P is calculated only from $\kappa_{\nu,\rm a}$. This weighting function peaks at $h\nu \simeq 2.8\, k_BT$, indicating where $\kappa_{\nu,\rm a}$ is most strongly sampled.

The Rosseland mean opacity κ_R yields the correct value for the integrated energy flux of an optically thick plasma

$$\frac{1}{\kappa_R} = \frac{\int_0^\infty \frac{1}{\kappa_{\nu,t}} \frac{dB_\nu(T)}{dT}\, d\nu}{\int_0^\infty \frac{dB_\nu(T)}{dT}\, d\nu}. \quad (2)$$

The use of a harmonic average means the individual contributions (bound–bound, bound–free, free–free, scattering) cannot be averaged first and then added to obtain the proper mean value. This weighting function peaks at $h\nu \simeq 3.8\ k_B T$, indicating where $\kappa_{\nu,t}$ is strongly sampled.

The radiation transport equation in the gray-diffusion approximation (e.g., Mihalas 1978)

$$\frac{\partial E_r}{\partial t} = \nabla \cdot \left(\frac{c/3}{\rho\kappa_R}\nabla E_r\right) + c\rho\kappa_P(aT_e^4 - E_r) \quad (3)$$

admits two mean free paths; $\lambda_R = 1/\rho\kappa_R$ (used in the diffusion coefficient term) and $\lambda_P = 1/\rho\kappa_P$ (used in the radiation–electron coupling term). The two mean free paths can differ by several orders of magnitude due to the different averaging prescriptions. Here E_r is the radiation energy, a is the radiation constant, and T_e is the electron temperature. In stellar evolution models, κ_R is used for the radiative temperature gradient

$$\nabla_{\rm rad} = \left(\frac{d\ln T}{d\ln P}\right)_{\rm rad} = \frac{3\kappa_R LP}{16\pi acGM_r T^4}, \quad (4)$$

where L is the luminosity, P is the pressure, G is the gravitational constant, and M_r is the mass contained within radius r. $\nabla_{\rm rad}$ in the mixing-length theory of convection (MLT) determines convective stability, the radiative flux in convective regions, and the actual temperature gradient in radiative regions.

Radiative opacities depend on the composition, which can change rapidly in mass or time due to nuclear reactions, diffusion, or chemical mixing. A typical approach is to adopt a fixed solar abundance mixture of metals with mass fraction Z, hydrogen mass fraction X, and helium mass fraction Y. Individual Rosseland mean opacity tables are calculated for various combinations of X and Z, where $Y = 1 - X - Z$, and the chemical elements that compose Z have a fixed distribution. Tabulated Rosseland mean opacity values computed with a fixed metal distribution are an acceptable alternative to calculating self-consistent Rosseland mean opacities that reflect the exact metal distribution of a stellar model as it evolves. The adoption of self-consistent Rosseland mean opacity tables results in a $\lesssim$2% change to the total opacity in a stellar model (Hui-Bon-Hoa 2021).

We use MESA's kap module to implement the new atomic radiative opacity tables and compare them to previous atomic opacity releases. The kap module builds opacity tables by combining the radiative opacities and electron-conduction opacities

$$\frac{1}{\kappa} = \frac{1}{\kappa_R} + \frac{1}{\kappa_{\rm cond}}, \quad (5)$$

where $\kappa_{\rm cond} = 16\sigma T^3/\rho K$ converts an electron conductivity K to an opacity. Electron-conduction opacities are tabulated for atomic charges $1 \leqslant Z \leqslant 60$ between $3 \leqslant \log T \leqslant 10$ and $-6 \leqslant \log\rho \leqslant 11.5$ (Cassisi et al. 2007; Blouin et al. 2020).

The cores of stellar models mostly evolve along lines of constant specific radiation entropy $S_{\rm rad} \sim T_c^3/\rho_c \sim M^2$ for a fixed nondegenerate stellar mass M. Atomic and molecular radiative opacities in MESA are tabulated using the conventional OPAL $\log R - \log T$ format, where $R = \rho/T_6^3$ which scales as $\sim 1/S_{\rm rad}$. The advantage of using $T_6 = T/10^6$ K and R is that the range of interest for stellar physics can be covered by a rectangular array in these variables (Bahcall & Ulrich 1988).

Molecular transitions (e.g., H_2, H_2O, TiO, CO) are the primary source of the radiative opacity for $\log T \leqslant 4.5$. In this regime, the kap module provides radiative opacities from Ferguson et al. (2005). The kap module also supplies a privately communicated set of Freedman et al. (2008) low-temperature opacities, and supports ÆSOPUS opacities (Marigo & Aringer 2009) for arbitrary chemical mixtures (see Jermyn et al. 2023, for details). MESA currently defaults to blending the higher-temperature and lower-temperature opacity tables between $3.80 \leqslant \log T \leqslant 3.88$ (see Paxton et al. 2013). Compton scattering dominates the radiative opacities for $\log T \geqslant 8.7$, where the kap module uses Poutanen (2017). For intermediate temperatures, atomic radiative opacities have been supplied by OPAL (Iglesias & Rogers 1993, 1996) and OP (Badnell et al. 2005; Seaton 2005). Type-1 OPAL tables, the subject of this article, have a fixed heavy element metal distribution (e.g., H burning). Type-2 OPAL tables provide radiative opacities for C- and O-rich mixtures (e.g., He burning; Iglesias & Rogers 1993).

2.1. OPLIB Database

The Los Alamos OPLIB opacity database has been publicly available for more than 40 years and is currently accessible at the website http://aphysics2.lanl.gov/opacity/lanl. The database contains monochromatic opacities for the first 30 elements of the periodic table, using a photon-energy grid of 14,900 points in the variable $u = h\nu/k_B T$, with values ranging from $10^{-4} \leqslant u \leqslant 30{,}000$. The website can produce monochromatic, multigroup, and gray opacities for either pure elements or arbitrary mixtures. The most recent database release (Colgan et al. 2016), which is referred to simply as "OPLIB" in the comparisons provided in this article, was generated with the ATOMIC code, while the previous release, which is referred to as "OPLIB-L," was generated with the LEDCOP code (Magee et al. 1995).

Since this article focuses on the latest OPLIB release, which is intended to supersede the OPLIB-L release, we provide a brief summary of the relevant computational methods. ATOMIC is a multipurpose plasma modeling code (Magee et al. 2004; Hakel et al. 2006; Fontes et al. 2015) that can be run in local thermodynamic equilibrium (LTE) or non-LTE mode to calculate the atomic-state populations. In this article, we focus on LTE populations. These populations are combined with atomic data, e.g., oscillator strengths and photoionization cross sections, to obtain the monochromatic opacities, which are constructed from the standard four contributions: bound–bound, bound–free, free–free, and scattering.

When calculating the populations, ATOMIC uses the ChemEOS model to account for the effects of the plasma environment on the equation of state (Hakel & Kilcrease 2004; Hakel et al. 2006; Kilcrease et al. 2015). While OPAL is based on the physical picture that treats plasma as a collection of nuclei and electrons Coulomb-interacting in the grand canonical ensemble, ChemEOS uses the chemical picture in

which the free electrons and the various ion stages are identified as individual species in the canonical ensemble; the associated Helmholtz free energy is then minimized in ChemEOS to yield the species' populations. From that perspective, ChemEOS is similar to OP, with which it also shares the use of occupation probabilities to model the gradual dissolution of ion stages' bound states by the plasma environment. ChemEOS differs from OP in the precise form of the occupation probabilities due to its adopted plasma microfield model and in the details of excluded-volume considerations for the ion stages' finite sizes. Furthermore, in order to extend the validity of the chemical picture to high densities ChemEOS adopts a model for the species' Coulomb interactions that smoothly bridges the transition from the Debye–Hückel limit at low densities to the Thomas–Fermi limit in the strongly coupled high-density regime.

For the latest OPLIB release, `ATOMIC` used semi-relativistic Hartree–Fock atomic data that were generated with the Los Alamos suite of atomic physics codes (Fontes et al. 2015). Improvements over the previous (`LEDCOP`) OPLIB release include the addition of 24 isotherms to reduce interpolation errors, extending the calculations to higher densities, and the inclusion of significantly more lines via a histogram method (Abdallah et al. 2007). Additional details about the latest OPLIB release, as well as comparisons with other opacity databases, are provided in Colgan et al. (2016). These improvements have made possible the generation of higher-fidelity opacity tables for pretabulated (X, Y, Z) mixtures of interest, as compared to the pretabulated OPLIB-L tables publicly available at http://aphysics2.lanl.gov/opacity/lanl. We detail these improvements in the next section.

Before leaving this section, we provide some general information about uncertainties in the calculated opacities. Uncertainties in the Rosseland mean opacity are caused by uncertainties in the calculation of the fundamental atomic cross sections, plasma effects caused by perturbing ions, and computational limitations. For example, measurements of fundamental cross sections are usually carried out on neutral atoms, rather than on charged ions, due to the difficulty in preparing a sample in a specific ion stage and because of the myriad possibilities of excited levels. On the other hand, the cross sections of neutral atoms are more difficult to calculate accurately because of the many-body, electron–electron interactions. Thus, a comparison of calculations with measured cross sections for neutral species can provide an upper bound on cross-section uncertainties. For Sun-like conditions, estimates of the uncertainty in the opacity are $\simeq$5% when electron scattering dominates at high T and low ρ (Huebner & Barfield 2014). As ρ increases and free–free processes become more important, the uncertainty is less than $\simeq$10%. As T decreases and bound–free processes become important, the uncertainty increases to $\simeq$20%. As T decreases further, bound–bound processes can contribute, and the uncertainty rises to $\simeq$30% (Huebner & Barfield 2014). From atomic theory considerations, the uncertainties in the calculated cross sections, particularly those that involve bound electrons, progressively decrease as the ionic charge increases toward the limiting case of one-electron (hydrogenic) ions, provided that plasma effects do not become too important. Such conditions exist for a variety of astrophysical applications, such as the solar modeling discussed in Section 3.

2.2. New OPLIB Opacity Tables

Figure 1 shows the OPLIB tables in the X–Z plane (left panel). Previous opacity releases by OP and OPAL contain 126 tables spanning $Z = 10^{-4}$ to $Z = 0.1$, and $Z = 0.0$. We have improved on these grids in three ways. First, we expand the range to $Z = 10^{-6}$ to $Z = 0.2$, allowing for improved accuracy of opacities at low and high Z. Second, we substantially increase the table density in the range $Z = 10^{-4}$ to $Z = 0.1$ enhancing the accuracy of opacities drawn from interpolations across neighboring metallicities. Third, we add opacity tables between $X = 0$ and $X = 0.1$. The addition of tables at $X = 10^{-2}$, 10^{-3}, 10^{-4}, 10^{-5}, and 10^{-6} can, for example, improve stellar models with thin H-depleted mixtures, such as in the atmospheres of hot subdwarfs or other stripped stars. These new OPLIB tables encompass 1194 individual tables, an order of magnitude larger in number than any previous opacity table release, and span regimes where previous opacity tables have not existed.

Figure 1 also shows the OPLIB tables in the $\log T$–$\log R$ plane (right panel). OP and OPAL radiative opacity tables are tabulated for $3.75 \leqslant \log(T/\mathrm{K}) \leqslant 8.7$, and $-8 \leqslant \log(\mathrm{R}) \leqslant 1$, with 70 tabulated points in $\log(T/\mathrm{K})$ and 19 tabulated points in $\log(R)$. The new OPLIB radiative opacity tables are tabulated over a larger space of $3.764 \leqslant \log(T/\mathrm{K}) \leqslant 9.065$, and $-8 \leqslant \log(R) \leqslant 1.5$ with 74 tabulated points in $\log(T/\mathrm{K})$ and 39 tabulated points in $\log(R)$. Table values are written to four decimal place precision, an improvement over other works which write values to three decimal place precision. Each opacity table is calculated with a mixture of 25 elements: H, He C, N, O, F, Ne, Na, Mg, Al, Si, P, S, Cl, Ar, K, Ca, Sc, Ti, V, Cr, Mn, Fe, Co, Ni.

2.3. OPLIB Opacity Tables in `MESA`

The 126 OPAL and OP opacity tables are preprocessed via smoothing and spline-fitting routines provided in Seaton (1993) to ensure smooth opacity derivatives. When run through these routines, OP and OPAL tables are smoothed and interpolated from 70 $\log(T/\mathrm{K})\times 19$ $\log(R)$ point tables spanning $3.75 \leqslant \log(T/\mathrm{K}) \leqslant 8.70$ and $-8.0 \leqslant \log(R) \leqslant 1.0$ into evenly spaced 138 $\log(T/\mathrm{K})\times 37$ $\log(R)$ opacity tables using bicubic splines. We take a similar approach by applying bicubic splines without a smoothing filter to the OPLIB tables, which interpolates our 74 $\log(T/\mathrm{K})$ points up to 213 points. Further discussion of the interpolation method along with comparisons between the raw and interpolated tables are provided in Appendix A.

`MESA`'s `kap` module computes the radiative opacity given ρ, T, X, Z from a cell. For a fixed composition opacity table in the X–Z plane, `MESA` interpolates between ρ and T values with an on-the-fly bicubic spline. The spline returns $\kappa_R(\rho, T)$, and its partial derivatives, $\partial\kappa_R(\rho, T)/\partial T$ and $\partial\kappa_R(\rho, T)/\partial\rho$.

`MESA` currently offers two choices for interpolating between opacity tables in X–Z: linear or monotonic Hermite cubic spline functions (see Paxton et al. 2011). The default is linear interpolation, as exemplified in `MESA`'s test suite (Wolf et al. 2023). In this article we activate cubic interpolation in `MESA`'s inlist controls to return $\kappa_R(\rho, T, X, Z)$:

```
cubic_interpolation_in_X = .true.
cubic_interpolation_in_Z = .true.
```

Appendix B explores the impact of adopting cubic versus linear interpolation of opacity data tables across X–Z in `MESA`. We find that linear interpolation systematically underpredicts

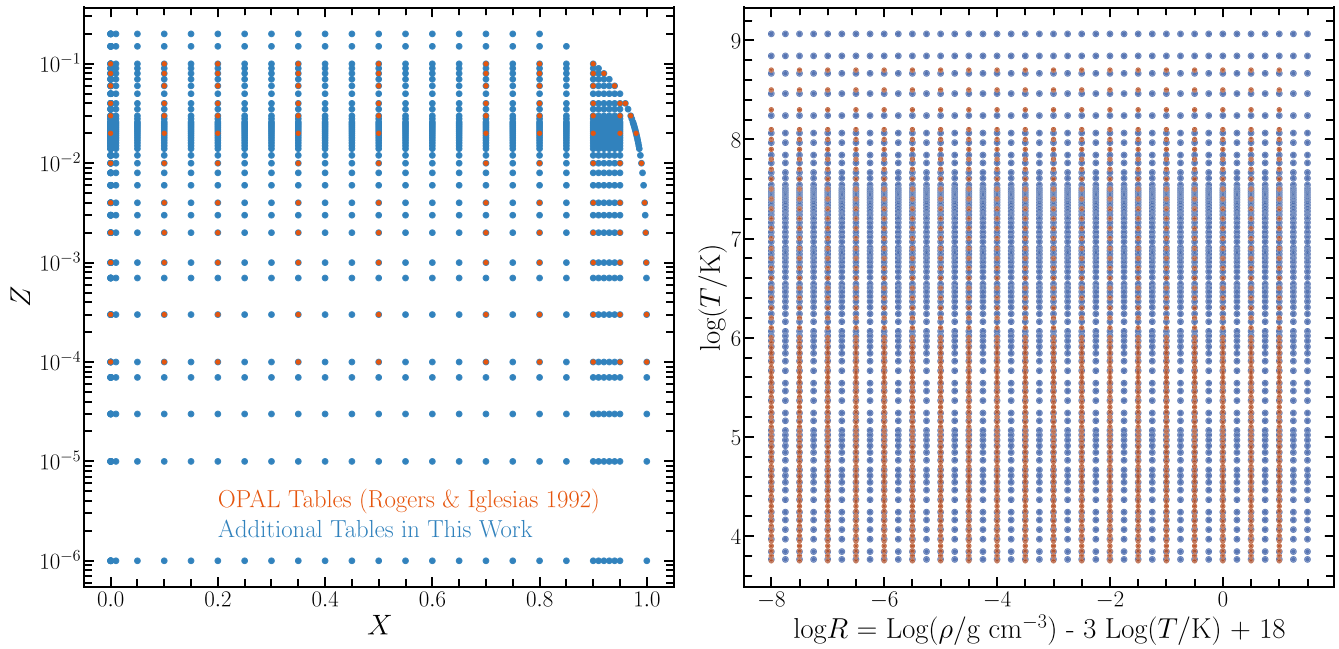

Figure 1. Location of each Type-1 opacity table in the X–Z plane (left panel) and the $\log T$ –$\log R$ plane (right panel). Orange circles mark the location of the 126 OPAL Type-1 tables (Rogers & Iglesias 1992). Blue circles mark the location of the new 1194 Type-1 opacity tables.

the opacity as compared to cubic interpolation, and recommend cubic interpolation be activated when using MESA. We leave further exploration and improvements to MESA's opacity interpolation methods to future work.

Figure 2 shows κ and its partial derivatives $\partial\kappa/\partial T$ and $\partial\kappa/\partial\rho$ generated by the OPLIB radiative opacities and MESA's kap module for an $X = 0.7$, $Z = 0.02$ Grevesse & Sauval (1998) abundance mixture. The left column shows these quantities as a function of T for different ρ. The dependence of κ with T in the upper left plot can be approximated with three temperature ranges. At low temperatures, $\log(T/\mathrm{K}) \lesssim 4$, the H^- opacity dominates and scales as $\kappa \sim \rho^{1/2}T^9$ (Hansen et al. 2004) as shown by the labeled dotted black line in the upper left plot of Figure 2. At higher temperatures, $4 \lesssim \log(T/\mathrm{K}) \lesssim 8$, the free–free (inverse thermal bremsstrahlung) and bound–free (radiative recombination) opacity dominates and scales as $\kappa \sim \rho T^{7/2}$ (Kramers 1923; Gaunt 1930) also shown by a labeled dotted black line. At still higher temperatures, $\log(T/\mathrm{K}) \gtrsim 8$, all the opacity curves converge to $\kappa \sim$ constant, the flat plateau at the foot of the "κ mountain" (Kippenhahn & Weigert 1990). When the atoms are completely ionized, then there are only two sources of opacity, free–free and Compton scattering. For low densities, Compton scattering dominates κ_R and does not impact κ_P. For high densities, free–free transitions dominate κ_R and κ_P.

Two additional features of the κ curves in the upper left plot of Figure 2 are noteworthy. The first is that the location of peak κ shifts toward higher T as ρ increases. The H^- opacity depends on the abundance of neutral hydrogen. A pure atomic H composition is 1/2 ionized by the Saha equation when (Hansen et al. 2004)

$$\rho = 8.02 \times 10^{-9}\, T^{3/2} \exp(-1.578 \times 10^5/T). \quad (6)$$

This locus of points is shown by the black circles and reflects the broad trend in the location of peak κ, where the dominant opacity smoothly transitions from H^- to bound–free. The second feature is the Fe group opacity bump (or Z bump) at $\log(T/\mathrm{K}) \simeq 5.35$, centered in the colored region denoting the thermal ionization regime of Fe, most prominent at low densities (blue curves).

The standard solar model shown in the upper left plot of Figure 2, which is detailed in Section 3, begins at the photosphere on the left with $\log(T/\mathrm{K}) = 3.762$ and $\log(\rho/\mathrm{g\ cm^{-3}}) = -6.66$. Progressing inward, toward higher T, the opacity sharply increases due to ionization of elements with low-lying first ionization stages (e.g., Na, Mg, Al, K, Ca, and H). These stages provide electrons for H^- formation, and κ rises by several orders of magnitude until it reaches a maximum at approximately the half-ionization curve for pure H when most H is ionized and thus is not available for H^- formation (Kippenhahn & Weigert 1990; Hansen et al. 2004). Progressing further inward, bound–free transitions become the main source of opacity, and still further inward free–free transitions dominate. The solar core remains in the domain of free–free transitions (Kippenhahn & Weigert 1990).

The upper right plot of Figure 2 shows contours of κ in the $\rho - T$ plane over a larger range of T and ρ than in the corresponding upper left plot. The red κ mountain is prominent. The overlaid standard solar model profile shows that high-energy photons generated in the solar core follow one trajectory in traversing the face of the κ mountain before eventually being released as lower-energy photons at the photosphere. Another face of the κ mountain, toward larger ρ, is bounded by the region where κ_{cond} dominates the opacity. Note the $\log(R) = 1.5$ opacity tables define the peak of the κ mountain.

The partial derivatives of the opacity with respect to temperature $\partial\kappa/\partial T$ and with respect to density $\partial\kappa/\partial\rho$ are useful for assessing excitation of a κ mechanism (Saio 1993)

$$\frac{d}{dr}\left(\frac{\partial\kappa}{\partial T} + \frac{\partial\kappa}{\partial\rho}\frac{1}{\Gamma_3 - 1}\right) > 0, \quad (7)$$

where $\Gamma_3 \equiv d\ln T/d\ln\rho|_S + 1$ is the third dimensionless adiabatic exponent from the equation of state. Opacity

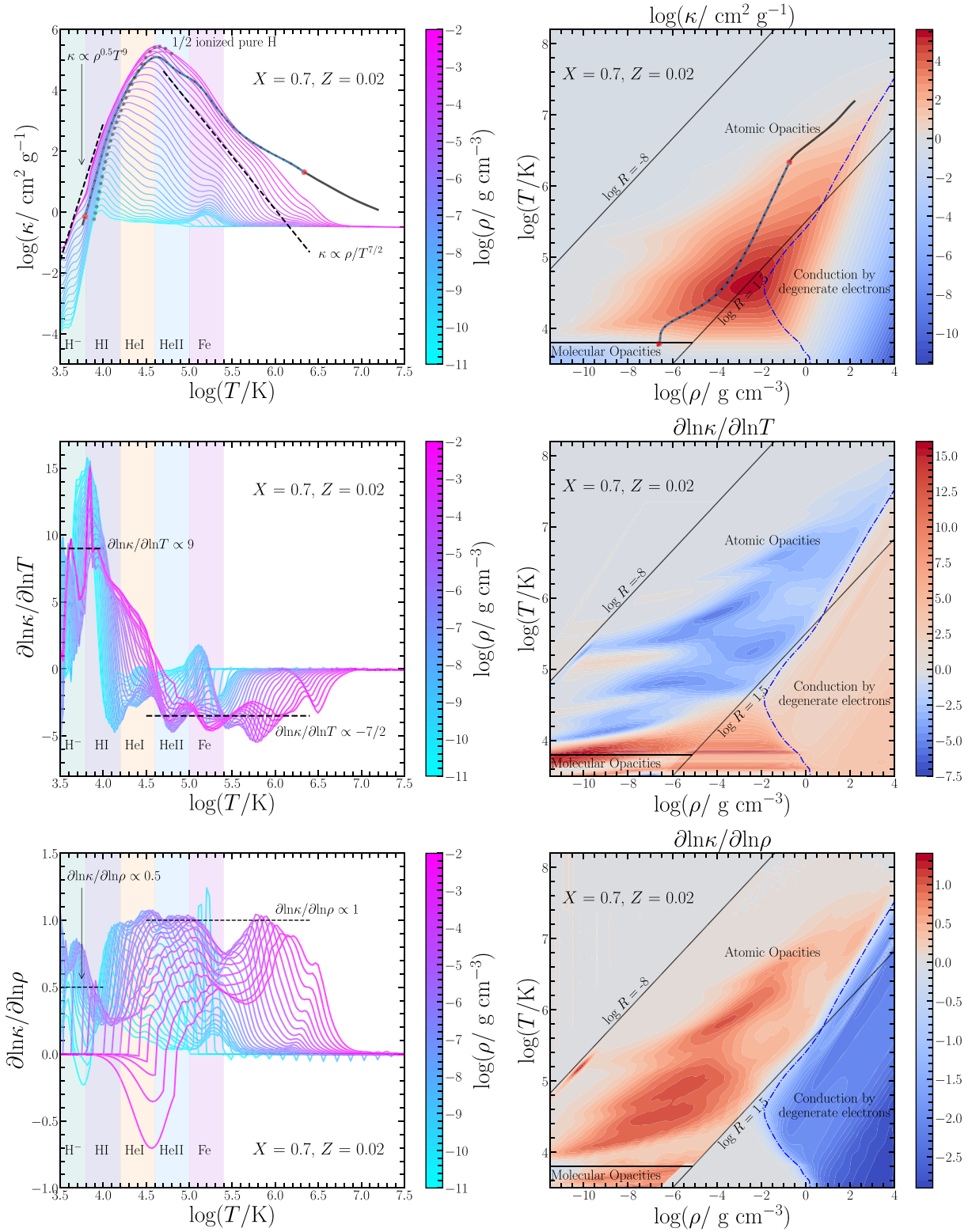

Figure 2. Opacities and partial derivatives with respect to the temperature and density for a $X = 0.7$, $Z = 0.02$ Grevesse & Sauval (1998) abundances generated from OPLIB radiative opacities and MESA's `kap` module. Left column: These quantities as a function of T for different ρ (color bar). Dashed black lines show scaling relations for H^- and Kramers opacities. Black dots mark the locations where a pure H composition is 1/2 ionized. Colored regions show the thermal ionization stages of key elements for nondegenerate material. Right column: These quantities as contours in the $\rho - T$ plane. Regions, where different opacity sources dominate, are labeled, as are the $\log R = -8$ and $\log R = 1.5$ table limits of the OPLIB radiative opacities. Both columns: Black curves show the profile of a standard solar model (see Section 3). Red circles on the solar profile mark the inner and outer boundaries of the convective region and are connected with a dashed blue curve.

derivatives are also useful for constructing the Jacobian matrix of derivatives for Newton-like iterations to solve the stellar evolution hydrodynamic equations.

The middle row of Figure 2 shows $\partial\kappa/\partial T$ and the bottom row shows $\partial\kappa/\partial\rho$ for this chemical mixture. The left column shows these quantities as a function of T for different ρ, and the

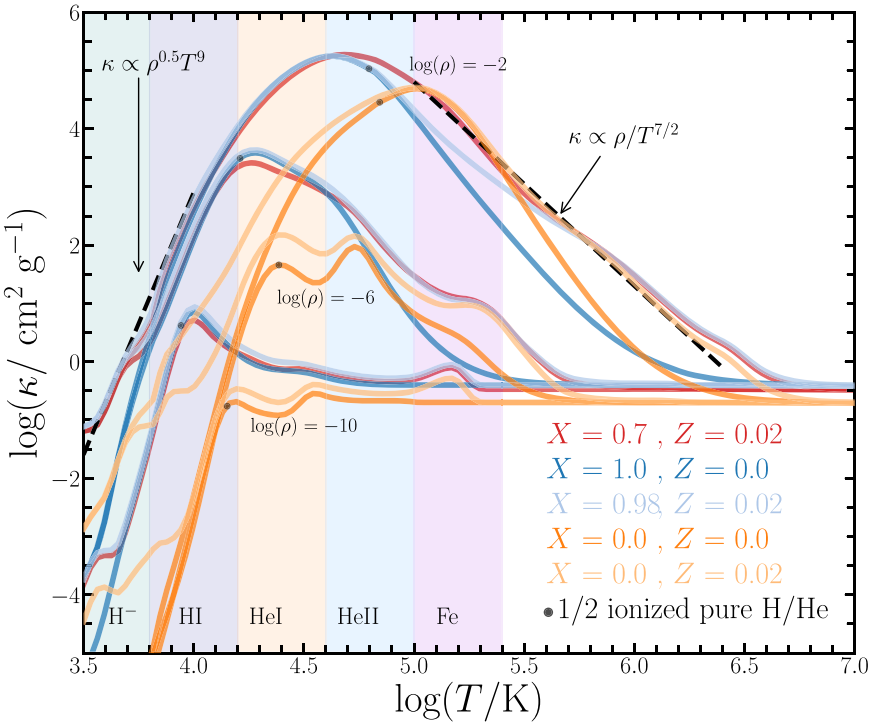

Figure 3. Opacity as a function of T for three values of $\log(\rho)$ (black labels) and five compositions with Grevesse & Sauval (1998) abundances (colored curves), generated from OPLIB radiative opacities and MESA's kap module. Dashed black lines show scaling relations for H^- and Kramers opacities. Black circles mark the half-ionization points for the pure atomic H composition (dark blue curves, Equation (6)) and the pure atomic He composition (dark orange curves, Equation (8)). Colored regions show the thermal ionization stages of key elements for nondegenerate material.

right column shows the contours of these partial derivatives in the $\rho - T$ plane. Peaks and changes in the slope of these four plots correlate with ionization stages due to the injection of additional electrons into the plasma. Examples include the onset of light metal ionization at low T and the ionization stages of H and He at larger T. The sign and magnitude of the partial derivative features are relevant for variable stars driven by the ionization stages of different elements (e.g., He ionization and RR Lyrae variables).

Figure 3 compares the κ generated from OPLIB radiative opacities and MESA's kap module at $\log(\rho/\mathrm{g\,cm^{-3}}) = -2$, -6, and -10 for five compositions: the same X and Z as in Figure 2, pure H, a solar Z with the remainder H, pure He, and a solar Z with the remainder He. We first analyze the three H-rich mixtures and then the two He-rich mixtures.

All three H-rich mixtures show a peak κ that shifts toward higher T as ρ increases, reflecting the half-ionization curve of H discussed in Figure 2. A difference occurs in κ between these three H-rich mixtures at $\log(T/\mathrm{K}) \lesssim 3.8$, reaching a 3 orders of magnitude difference for $\log(\rho/\mathrm{g\,cm^{-3}}) = -2$ at $\log(T/\mathrm{K}) = 3.5$. Here, the lack of electrons from metals with relatively low ionization potentials in the pure H composition (blue curve) delays the onset of a dominant H^- opacity until H ionizes. Another difference occurs at $\log(T/\mathrm{K}) \gtrsim 5.0$ for all three densities, where the lack of electrons from Fe group atoms in the pure H composition (blue curve) suppresses the bound–free and free–free opacities relative to the two mixtures with a solar complement of Fe.

Helium contributes four main opacity sources: He^- free–free (Somerville 1965; John 1994), He^{2+} bound–free, and free–free (Ignjatović et al. 2009), He Rayleigh scattering (Iglesias et al. 2002; Rohrmann 2018), and triple-He collision (Kowalski 2014; Blouin et al. 2019). The two He-rich mixtures in Figure 3 (orange curves) have opacities that are usually about an order of magnitude smaller for a given T and ρ than the opacities of the H-rich mixtures before electron scattering dominates. Below $\log(T/\mathrm{K}) \lesssim 4.2$, the presence of free electrons from the ionization of trace metals with relatively low ionization potentials introduces He^- free–free electron scattering and He_2^+ bound–free absorption that increases κ by several orders of magnitude in the He composition with solar Z (Saumon et al. 2022). Above $\log(T/\mathrm{K}) \gtrsim 5.0$ for all three densities, the lack of electrons from Fe group atoms in the pure He composition (dark orange curve) reduces the bound–free and free–free opacities relative to the mixture with a solar Fe abundance (light orange curve). The κ curves for $\log(\rho/\mathrm{g\,cm^{-3}}) = -2$, -6 show undulations due to He^0 in excited states, H^0 in its ground state and He^+ in excited states, and He^+ in its ground state (Seaton et al. 1994). Like the three H-rich mixtures, both He-rich mixtures also show a peak κ that shifts toward higher T as ρ increases. An approximate expression for the half-ionization curve for a pure atomic He mixture is

$$\rho = 4 \cdot 8.02 \times 10^{-9}\ T^{3/2}\ \exp(-2.853 \times 10^5 / T). \quad (8)$$

The half-ionization points for pure atomic H (Equation (6)) and pure atomic He (Equation (8)) mixtures are shown by the black circles in Figure 3. These approximations broadly reflect the trend, but miss the κ peaks due to missing physics in the approximations, for example, the abundance of H^- in a hydrogen mixture.

2.4. Verification of the OPLIB Opacities

Here we illustrate some differences between the 1194 OPLIB opacity tables, a degraded set of 126 OPLIB opacity tables, and the 126 OPAL opacity tables. Figure 4 shows the

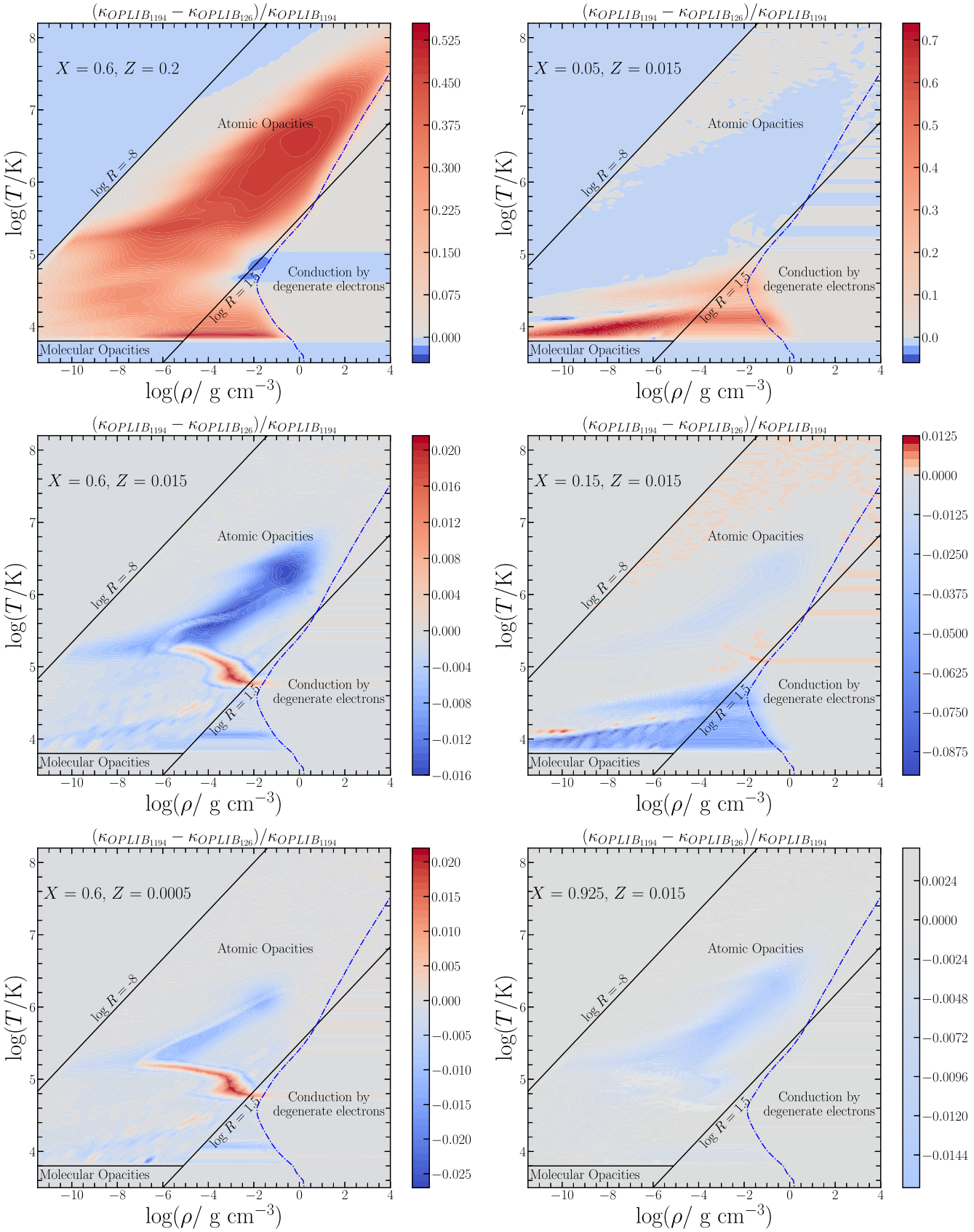

Figure 4. Relative differences between the 1194 OPLIB and 126 OPLIB opacity table grids using Grevesse & Sauval (1998) abundances, generated from MESA's kap module, for six mixtures. The left column shows mixtures with $X = 0.6$ and varying Z, and the right column shows mixtures with $Z = 0.015$ and varying X. The OPLIB $\log(R) = -8$, 1.5 table boundaries are marked with a solid black line. The approximate location of the Z-dependent transition to an electron-conduction-dominated opacity is marked with a dotted–dashed blue curve.

relative opacity differences between the OPLIB 1194 table grid (denoted $\kappa_{\rm OPLIB_{1194}}$) and the OPLIB 126 table grid (denoted $\kappa_{\rm OPLIB_{126}}$) for six mixtures in the $\rho - T$ plane. The six mixtures are chosen so that they lie between or outside the 126 OPLIB table grid in the X–Z plane. For constant $X = 0.6$ across $Z = 0.0005$, 0.015, 0.2, we find interpolation over the 1194 table grid results in a ≈2%–2.5% change in opacity over the 126 table grid for $Z \leqslant 0.1$. Since the 126 OPLIB opacity tables only reach $Z = 0.1$, MESA returns the opacity value at $Z = 0.1$ for $Z > 0.1$. For $Z = 0.2$ in the top left panel of Figure 4, the 1194 OPLIB tables provide improvements up to ≈50% in MESA. The right column of Figure 4 shows the opacity differences at $Z = 0.015$ across $X = 0.05$, 0.15, 0.925. We find interpolation over the 1194 OPLIB tables show a ≈2% change in the opacity at larger H mass fractions and up to 75% change in the opacity at smaller H mass fractions in the temperature range $3.8 \lesssim \log(T/{\rm K}) \lesssim 4.8$ due to the ionization of H and He. These differences are a direct result of the enhanced table density between $0 \leqslant X \leqslant 0.1$.

Figure 5 shows the opacity differences between the OPLIB 1194 tables and the OPAL 126 tables for six mixtures in the $\rho - T$ plane. In regions between the atomic radiative opacities and the conductive opacities with no table coverage, there can be large differences since MESA uses the values from the $\log(R)$ table edge and then extends/mixes these radiative opacities with the conductive opacities. Overall, we find differences between the 1194 OPLIB tables and the 126 OPAL tables extend from ≃20% at $X = 0.7$, $Z = 0.02$ to upward of 40%–80% for other mixtures, especially at low T and moderate ρ. In the case of the solar model profile shown in the left–middle panel at approximately solar metallicity, $X = 0.7$ and $Z = 0.02$, OPLIB opacity tables consistently predict a higher opacity at the base of the convective envelope and lower opacity in the Solar core at otherwise identical conditions.

3. Standard Solar Models

In this section, we detail the construction of standard solar models and their input physics. We quantify the resulting differences in their internal structure and compare them with observational helioseismic and neutrino flux constraints. Standard solar models have been previously calculated using OPLIB opacities in Colgan et al. (2016), Guzik et al. (2016), Raecke (2022), and OPLIB-L opacities by Neuforge-Verheecke et al. (2001b). We construct standard solar models with four differing photospheric estimates of the solar heavy element abundance: $Z/X = 0.0181$ (AGSS09; Asplund et al. 2009), $Z/X = 0.0229$ (GS98; Grevesse & Sauval 1998), $Z/X = 0.0187$ (AAG21; Asplund et al. 2021), and $Z/X = 0.0225$ (MB22; Magg et al. 2022). We compare solar models computed with OPLIB opacities to the default OP and OPAL opacity tables provided by MESA. We broadly find that standard solar models produced with OPLIB opacities have systematically lower core opacities and temperatures, and higher core densities resulting in lower neutrino fluxes and markedly different helioseismology than OP/OPAL models. We also find that standard solar models computed with higher-metallicity mixtures (GS98 or MB22) are in better agreement with helioseismic and neutrino constraints than low-metallicity mixtures (AGSS09 or AAG21) regardless of the adopted opacity table.

3.1. Input Physics

We use MESA version r22.11.1 to construct our stellar models (Paxton et al. 2011, 2013, 2015, 2018, 2019; Jermyn et al. 2023). Each star is modeled as a single, nonrotating, non-mass-losing, solar metallicity object. We use the built-in MESA nuclear reaction network mesa_28. Relatively large nuclear networks are required to fully capture the energy generation rate (Farmer et al. 2016), and thus, for example, the neutrino luminosity (Farag et al. 2024). The current defaults for nuclear reaction rates are described in Appendix A.2 of Paxton et al. (2019).

Rates are taken from a combination of NACRE (Angulo et al. 1999) and the Joint Institute for Nuclear Astrophysics REACLIB library (default version, dated 2017 October 20; Cyburt et al. 2010), supplemented with NACRE II reaction rates provided in Xu et al. (2013). We adopt the weak-decay rate for ^{7}Be from Simonucci et al. (2013). Note there is a long literature on the sensitivity of solar model neutrino fluxes to uncertainties in the nuclear physics (Bahcall & Ulmer 1996; Degl'Innoccenti et al. 1997; Bahcall & Pinsonneault 2004; Bahcall et al. 2006; Haxton & Serenelli 2008; Adelberger et al. 2011; Haxton et al. 2013; Vissani 2019; Villante & Serenelli 2021; Bellinger & Christensen-Dalsgaard 2022). The MESA screening corrections are from Chugunov et al. (2007), which includes a physical parameterization for the intermediate screening regime and reduces to the familiar weak (Dewitt et al. 1973; Graboske et al. 1973) and strong (Alastuey & Jancovici 1978; Itoh et al. 1979) limits at small and large values of the plasma coupling parameter. All the weak reaction rates are based (in order of precedence) on the tabulations of Oda et al. (1994), Langanke & Martínez-Pinedo (2000), and Fuller et al. (1985).

We use MESA's default equation of state (Jermyn et al. 2023), where a standard solar model's $\rho - T$ profile lies in the domain of FreeEOS calculated with a Grevesse & Sauval (1998) composition. The atmosphere is modeled using the solar-Hopf relation analytic fit by Ball (2021) to the Hopf function for the solar simulation by Trampedach et al. (2014).

We adopt the MESA default time-dependent convection model which reduces to the Cox MLT model (Cox & Giuli 1968) on long timescales typical of a solar model (Jermyn et al. 2023). We adopt the Ledoux criterion for convective stability, and we adopt a semiconvection efficiency coefficient of $\alpha = 0.1$. We use the convective premixing routine (Paxton et al. 2019) to determine the location of convective boundaries, and we do not include the effects of convective overshooting, rotational deformation, or the effects of rotational mixing. We include the effects of element diffusion for every isotope included in our nuclear network by solving the unmodified Burgers equations in cgs units and including the heat flow vector terms (Paxton et al. 2018). Each model is self-consistently evolved with the hydrodynamics such that a radial velocity variable is present throughout the evolution.

3.2. Standard Solar Model Calibrations

We perform solar model calibrations to generate standard solar models and compare our results with present-day helioseismic and neutrino observation data. We iterate on differences between the final model at $t_\odot = 4.568$ Gyr (Bouvier & Wadhwa 2010) and the solar radius, $R_\odot = 6.957 \times 10^{10}$ cm,

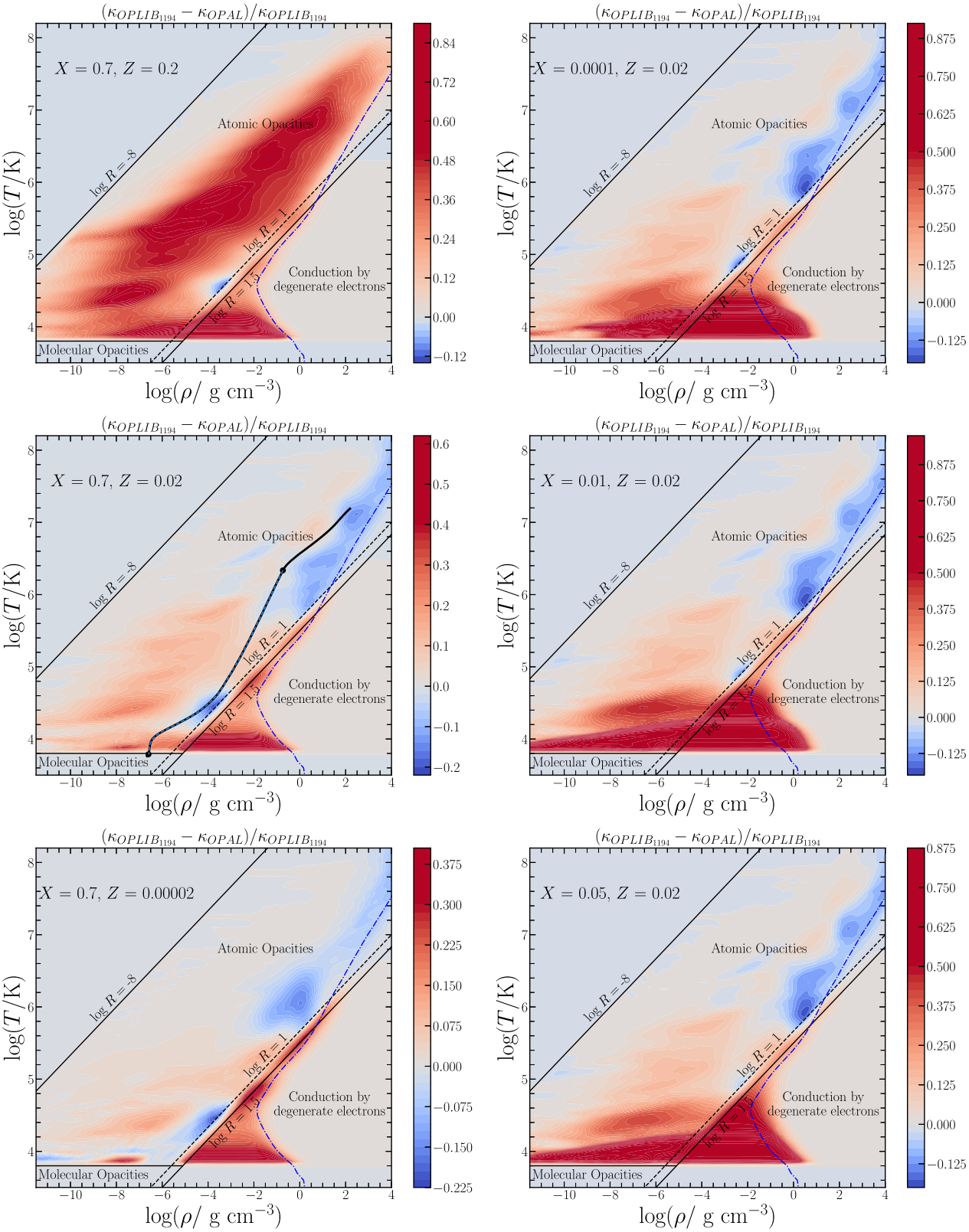

Figure 5. Relative differences between the 1194 OPLIB and 126 OPAL opacity table grids using Grevesse & Sauval (1998) abundances, generated from `MESA`'s `kap` module, for six mixtures. The left column shows mixtures with $X = 0.7$ and varying Z, and the right column shows mixtures with $Z = 0.02$ and varying X. The OP/OPAL $\log(R) = 1$ table boundary is marked with a dashed black line, the OPLIB $\log(R) = 1.5$ table boundary is marked with a solid black line, and the approximate location of the Z-dependent transition to an electron-conduction-dominated opacity is marked with dotted–dashed blue curve. The thick black curve for the $X = 0.7$, $Z = 0.02$ mixture marks the location of a standard solar model; the black dots mark the approximate beginning and end of the solar convection zone (overlaid blue dashed curve). Interpolation across the X–Z plane uses cubic splines.

Table 2
Solar Calibration Parameters and Properties

Component	X_0	Y_0	Z_0	$\alpha_{\rm mlt}$	$(Z/X)_{\rm surf}$	$L_{\nu,\odot}/L_{\gamma,\odot}$	$R_{\rm cz,b}/R_\odot$	$Y_{\rm surf}$
Currently in MESA								
OPAL_126 GS98	0.70964	0.27181	0.01855	1.799	0.0229	0.024181	0.718	0.24423
OPAL_126 AGSS09	0.71990	0.265125	0.01498	1.778	0.0181	0.023909	0.726	0.23697
OP_126 GS98	0.71114	0.27028	0.01857	1.810	0.0229	0.024133	0.718	0.24298
OP_126 AGSS09	0.72009	0.26490	0.01500	1.783	0.0181	0.023882	0.726	0.23674
From this Work								
OPLIB-L_126_50T GS98	0.71156	0.26975	0.01869	1.9054	0.0229	0.024150	0.7235	0.24186
OPLIB_126_50T GS98	0.71379	0.26762	0.01859	1.9494	0.0229	0.023977	0.7167	0.24108
OPLIB_126 GS98	0.71202	0.26944	0.01854	1.9442	0.0229	0.024010	0.7166	0.24275
OPLIB_126 AGSS09	0.72564	0.25931	0.01504	1.9403	0.0181	0.023679	0.7230	0.23258
OPLIB_126 AAG21	0.72654	0.25795	0.01551	1.9140	0.0181	0.023658	0.7214	0.23172
OPLIB_126 MB22	0.71480	0.26694	0.01826	1.9339	0.0225	0.023986	0.7151	0.24076
OPLIB_1194 GS98	0.71191	0.26955	0.01854	1.9437	0.0229	0.024012	0.7166	0.24284
OPLIB_1194 AGSS09	0.72607	0.25886	0.01507	1.9350	0.0181	0.023670	0.7248	0.23193
OPLIB_1194 AAG21	0.72684	0.25762	0.01554	1.9095	0.0181	0.023651	0.7225	0.23122
OPLIB_1194 MB22	0.71469	0.26705	0.01826	1.9331	0.0225	0.023988	0.7159	0.24082
Vinyoles et al. (2017)								
OP_126 GS98	0.7095	0.2718	0.0187	2.18	0.0229	⋯	0.7116	0.2426
OP_126 AGSS09met	0.7238	0.2613	0.0149	2.11	0.0187	⋯	0.7223	0.2317
Magg et al. (2022)								
OP_126 GS98	0.7095	0.2718	0.0187	⋯	0.0229	⋯	0.7122	0.2425
OP_126 AGSS09met	0.7237	0.2614	0.0149	⋯	0.0178	⋯	0.7231	0.2316
OP_126 AAG21	0.7207	0.2638	0.0155	⋯	0.0187	⋯	0.7197	0.2343
OP_126 MB22	0.7090	0.2734	0.0176	⋯	0.0225	⋯	0.7123	0.2439
Observation[a]	⋯	⋯	⋯	⋯	⋯	⋯	0.713 ± 0.001	0.2485 ± 0.0035

Note.
[a] The helioseismic derived radius at the bottom of the convective zone, $R_{\rm cz,b}$, and surface He mass fraction, $Y_{\rm surf}$, are from Basu & Antia (1997) and Basu & Antia (2004).

solar luminosity, $L_{\gamma,\odot} = 3.828 \times 10^{33}$ erg s^{-1} (Prša et al. 2016), and surface heavy element abundance Z/X.

We use the built-in MESA simplex module to iteratively vary the mixing-length parameter, α, and the initial composition X, Y, and Z. This calibration is performed for four estimates of the heavy element abundance at the surface of the Sun: $Z/X = 0.0181$ (AGSS09, Asplund et al. 2009), $Z/X = 0.0229$ (GS98, Grevesse & Sauval 1998), $Z/X = 0.0187$ (AAG21, Asplund et al. 2021), and $Z/X = 0.0225$ (MB22, Magg et al. 2022).

Calibrated parameters are listed in Table 2. The solar models are calculated using OPAL (Iglesias & Rogers 1996), OP (Badnell et al. 2005), OPLIB, and OPLIB-L (see Section 2.1) Rosseland mean radiative opacities.

Each of the 16 stellar models calculated in this work has approximately 5000 mass zones. Each model takes approximately 1200 time steps. Each model takes approximately 2–4 hours to run on a 12–16 core machine. Each solar model is run roughly 150–200 times to calibrate, taking roughly 2–4 weeks to complete. The MESA files to reproduce our models, along with the Python scripts to reproduce all of our plots are available at doi:10.5281/zenodo.10798600.

3.3. Helioseismic Observables

Helioseismic inversions of solar models in combination with solar oscillation data provide observational estimates of quantities such as the radius of the solar convection zone base (Christensen-Dalsgaard et al. 1991; Kosovichev 1993; Basu & Antia 1997), the convection zone helium mass fraction (Dziembowski et al. 1991; Vorontsov et al. 1991; Antia & Basu 1994a; Basu & Antia 1995; Richard et al. 1998), radial profiles of sound speed and density (Christensen-Dalsgaard et al. 1985; Antia & Basu 1994b) two-dimensional profiles of the rotational velocity (Brown & Morrow 1987; Thompson et al. 1996), and other quantities such the Ledoux discriminant profile (Buldgen et al. 2020). In this section, we compare inferred helioseismic quantities from Basu & Antia (1997, 2004) and Basu et al. (2009) with those predicted by standard solar models with (GS98, AGSS09, AAG21, and MB22) abundances and (OPLIB, OPAL, and OP) opacity tables.

Calculated helioseismic quantities are shown in Table 2 for each set of opacity tables considered in this work and from Vinyoles et al. (2017) and Magg et al. (2022). Since we have evolved these solar models with otherwise identical input physics, disagreements between models of identical chemical mixtures should arise from differences in the treatment of atomic opacities. In Appendix C, we highlight the necessity of adopting cubic interpolation across X–Z in MESA to reproduce similar helioseismic results found in the other works.

The first column of Table 2 uses the notation "Source_N," where "Source" is OPLIB, OPAL, or OP and "N" is either 126 or 1194 signifying the number of individual tables. With two exceptions, all the models shown in Table 2 use an individual κ table resolution described in Section 2.2. The two exceptions are entry OPLIB_126_50T which refers to a calibrated solar model computed with 126 individual OPLIB tables at a table resolution of 50 temperature points, and entry OPLIB-L_126_50T which uses the older OPLIB-L tables at a table resolution also of 50 temperature points.

Table 2 also lists the initial abundances X_0, Y_0, and Z_0 along with the calibrated dimensionless mixing-length parameter $\alpha_{\rm mlt}$, the surface metal to H abundance ratio $(Z/X)_{\rm surf}$, the neutrino luminosity $L_{\nu,\odot}/L_{\gamma,\odot}$, the radius of the convection zone base $R_{\rm cz,b}/R_\odot$, and the surface helium mass fraction $Y_{\rm surf}$. We find both OP GS98 and AGSS09 MESA solar models agree well with the results found in both Vinyoles et al. (2017) and Magg et al. (2022), both of which use the GARSTEC (GARching STEllar Code, Weiss & Schlattl 2008) with the most up to date physical prescriptions from the "B16" solar models. These MESA models adopt the photospheric AGSS09 abundance mixtures. Vinyoles et al. (2017) and Magg et al. (2022) adopt the AGSS09 photospheric abundance mixture supplemented by meteoric abundances for refractory elements (labeled "AGSS09met" in Table 2). Some of the differences between the MESA OP AGSS09 and the Vinyoles et al. (2017) OP AGSS09met models can be attributed to these composition differences. Overall, OPLIB standard solar models produce a smaller $R_{\rm cz,b}/R_\odot$ and smaller $Y_{\rm surf}$ as compared to OP or OPAL solar models for similar compositions.

Figure 6 shows the fractional difference in sound speed, δc_s, for each calibrated solar model in Table 2 with respect to the helioseismic sound speeds inferred in Basu et al. (2009). The OPLIB-L_126_50T model in the top panel (blue curve) agrees more with OP and OPAL models (gray and purple curves respectively) in the stellar core for $r/R_o \lesssim 0.4$ but has a significantly larger δc_s as compared to the OPLIB, OP, or OPAL solar models for $r/R_o \gtrsim 0.4$. The OPLIB_126_50T model (red curve) shows similar sound speeds to OPLIB_126 (green curve) showing that the improved individual table resolution in the OPLIB_126 model does not have a measurable large impact on δc_s. The three OPLIB models have higher sound speeds compared to the OP, OPAL, and OPLIB-L models for $r/R_o \lesssim 0.2$, and lower sound speeds for $0.2 \lesssim r/R_o \lesssim 0.4$. In the envelope for $r/R_o \gtrsim 0.4$ the three OPLIB models are closer to the OP and OPAL models, yet show a difference in δc_s.

The AGSS09 mixture in the middle panel shows improvement in δc_s with OPLIB opacities (dark and light blue curves). The AAG21 and MB22 mixtures with OPLIB opacities in the bottom panel show overall better agreement with the inferred solar sound speed than the GS98 and AGSS09 mixtures.

Near the peaks in δc_s, below the convection zone base, the 1194 OPLIB models have a larger δc_s than the 126 OPLIB models for the AGSS09 and AAG21 mixtures (second and third panels) due to a lower opacity from the more accurate interpolations offered by the 1194 table set. The difference is more pronounced for the AGSS09 and AAG21 mixtures due to their lower metallicity, with $Z_0 \sim 0.015$ as opposed to $Z_0 \sim 0.018$–0.019 in the GS98 and MB22 mixtures where using 1194 or 126 tables has little consequence. A metallicity of $Z_0 \sim 0.015$ lies between the $Z \sim 0.01$ and $Z \sim 0.02$ tabulations of the default 126 table set. The new 1194 table set provides tables at $Z \sim 0.014$, 0.015, 0.016.

Figure 7 compares the κ, T, and ρ profiles of standard solar models evolved with GS98 and AGSS09 mixtures. The differences are normalized to standard solar models computed with OP opacities (Badnell et al. 2005), as they are commonly adopted standards in solar modeling studies. Models evolved with OPLIB opacities (blue curves) have ∼6%–7% lower core opacity than OP (dashed horizontal line) over $r/R_o \lesssim 0.15$, while the model with OPAL opacity (purple curve) is within

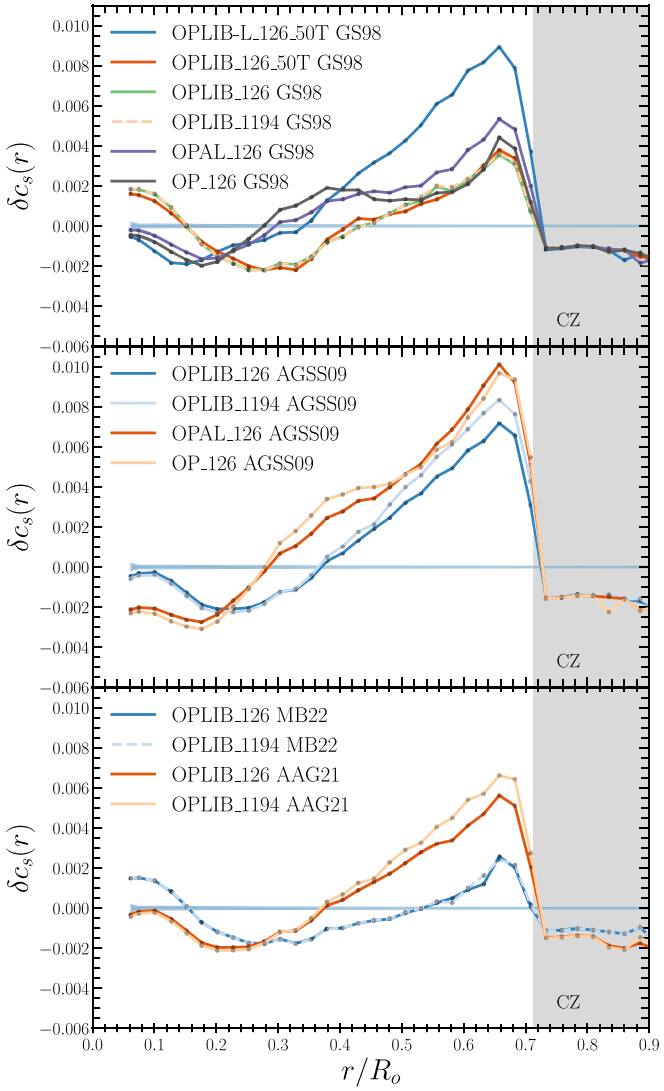

Figure 6. Fractional sound speed differences $\delta c_s = (c_{\rm obs}$ - $c_s(r))/c_s(r)$ between values predicted by a calibrated MESA standard solar model $c(r)$ and $c_{\rm obs}$ values inferred from helioseismic data (Basu et al. 2009). The 1σ observational uncertainties are shown as the blue bands at ordinates of zero. The top, middle, and bottom panels are for GS98, AGSS09, and MB22+AAG21 mixtures respectively. Black circles mark locations where δc_s is evaluated. Gray bands show the convective regions, labeled CZ.

∼1% of OP across the entire radiative core. Between $0.15 \lesssim r/R_o \lesssim 0.4$ the OPLIB normalized opacity difference decreases to a local minimum near $r/R_o \sim 0.4$, and increases to ∼3% at $r/R_o \sim 0.65$ below the convection zone base.

Differences in κ arising from the number of OPLIB tables adopted are visible in Figure 7 at $r/R_o \gtrsim 0.7$ for the GS98 and $r/R_o \gtrsim 0.5$ for AGSS09 mixtures. Overall, we find differences in the opacity table source (OP, OPAL, OPLIB) result in solar model opacity differences of ≈8% and ≈15% at the bottom and top of the solar convection zone, and up to ≈7% in the solar core. It should be noted that only a small portion of the total luminous flux in a convective envelope is carried by radiation; hence its structure is primarily determined by the EOS, not the opacity. However, opacity differences are important near the bottom and top of the solar convection zone, because the convective boundary location is where adiabatic and radiative temperature gradients are comparable to one another. The opacity is important in the shallow

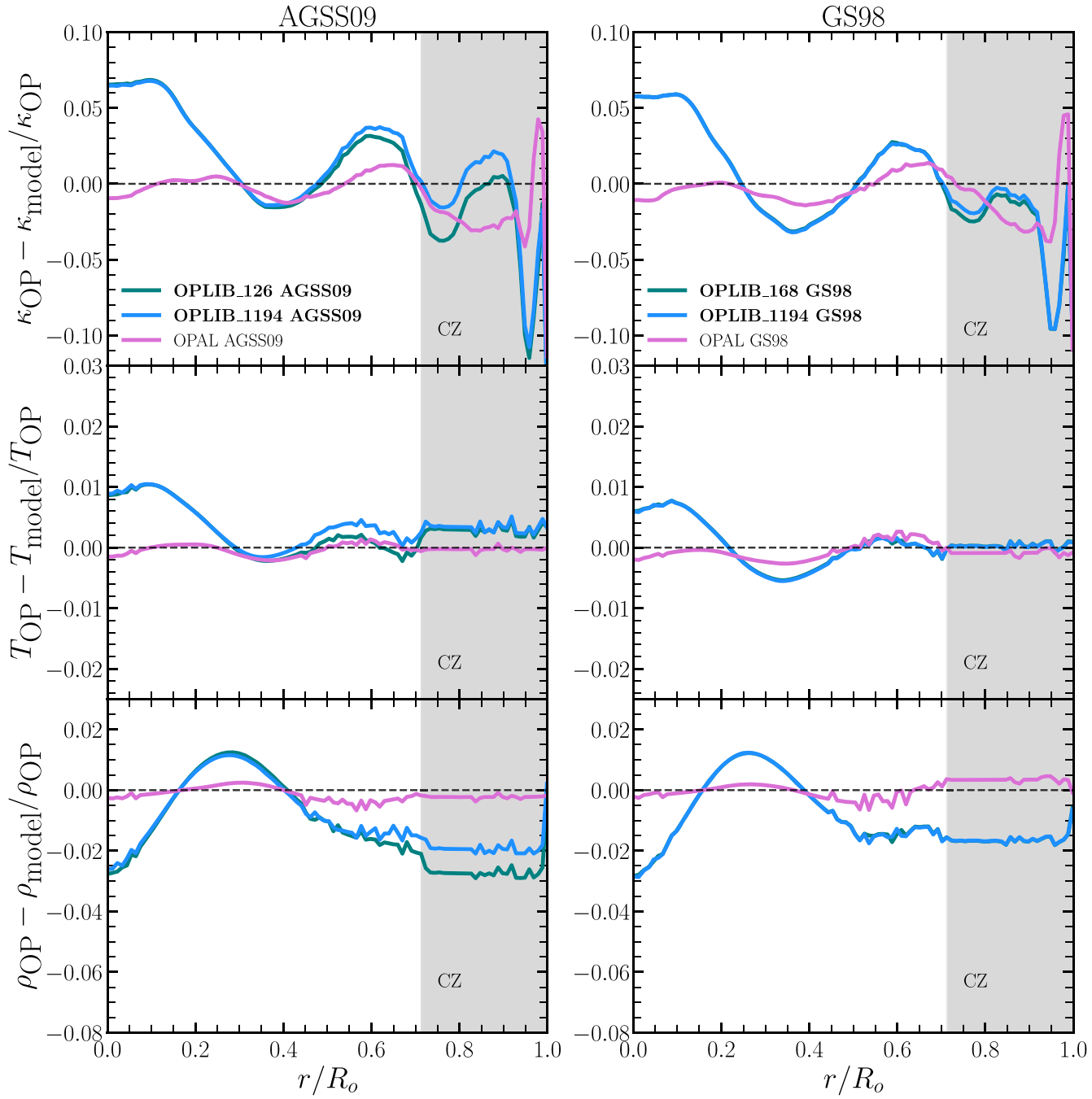

Figure 7. Opacity (top), temperature (middle), and density (bottom) differences between standard solar models normalized to a standard solar model computed with OP opacities (Badnell et al. 2005). The left column is for the Asplund et al. (2009) mixture and the right column is for the Grevesse & Sauval (1998) mixture. New results are labeled in bold font. We use a smoothing floor to reduce the noise generated by taking finite differences between small changes in radii.

superadiabatic layers, as it sets the entropy gradient for the convection zone as a whole, as well as the radiative atmosphere. In more massive, hotter stars than the Sun, these opacity differences can become very important because their envelopes can become radiation-dominated and are not always fully convective.

Standard solar models with the OPAL and OP tables have T and ρ profiles that are within 0.1% of one another, while models with the OPLIB opacities have 0.8%–1% lower T and 2.5%–3% higher ρ in the core. Outside of $0.2 \leqslant r/R_o \leqslant 0.4$ OPLIB solar models show $\gtrsim$1%–2% lower ρ than OP/OPAL solar models.

Figure 8 shows the fractional difference in sound speed and density between calibrated solar models and inferred helioseismic values (Basu et al. 2009). Models using the 1194 OPLIB table set are compared to models using the OP and OPAL tables across different initial compositions. Overall, the MB22 model shows the smallest δc_s and $\delta\rho$ differences. This suggests a high-Z solution to the solar model problem (Guzik 2008; Serenelli et al. 2009; Guzik & Mussack 2010; Salmon et al. 2021). Recent helioseismic determination of the solar mass fractions by Buldgen et al. (2023, 2024) favors low-Z mixtures such as AAG21. However, these two results are not necessarily in tension as the model sets are constructed and calibrated differently.

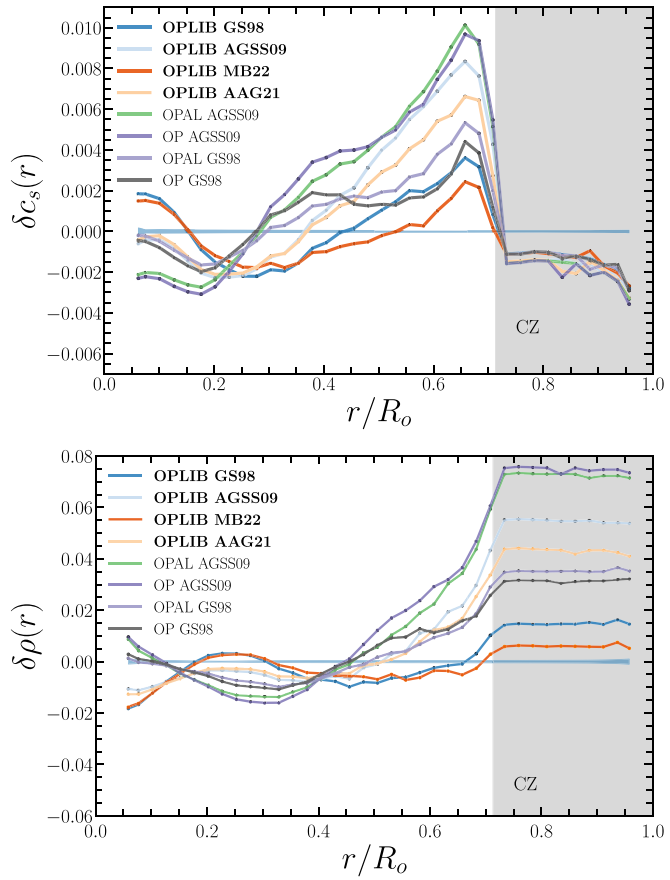

Figure 8. Fractional sound speed and density differences, $\delta c_s = (c_{\rm obs}$ - $c_s(r))/c_s(r)$ and $\delta\rho = (\rho_{\rm obs}$ - $\rho(r))/\rho(r)$, between the values predicted by a calibrated MESA standard solar model, $c_s(r)$ and $\rho(r)$, and the $c_{\rm obs}$ and $\rho_{\rm obs}$ values inferred from helioseismic data (Basu et al. 2009). The 1σ observational uncertainties are shown as the blue bands at ordinates of zero. Black circles mark locations where δc_s and $\delta\rho$ are evaluated. Gray bands show the convective regions, labeled CZ. New results are labeled in bold font.

3.4. Solar Neutrino Fluxes

Neutrinos are produced during H burning on the main sequence from the proton–proton chain reactions p(p,$e^+\nu_e$)^{2}H, p(e^-p,ν_e)^{2}H, ^{3}He(p,$e^+\nu_e$)^{4}He, ^{7}Be(e^-,ν_e)^{7}Li, ^{8}B(,$e^+\nu_e$)^{8}Be, and the CNO cycle reactions ^{13}N(,$e^+\nu_e$)^{13}C, ^{13}N(e^-,ν_e)^{13}C, ^{15}O(,$e^+\nu_e$)^{15}N, ^{15}O(e^-,ν_e)^{15}N, ^{17}F(,$e^+\nu_e$)^{17}O, ^{17}F(e^-,ν_e)^{17}O, ^{18}F(,$e^+\nu_e$)^{18}O, where electron capture reactions on CNO nuclei are included (Stonehill et al. 2004). The neutrino flux in the solar interior is strongly dependent on the core T (see Bahcall & Ulmer 1996). Standard solar models that accurately predict the T profile of the solar core should also generate comparable neutrino fluxes to solar neutrino data (Farag et al. 2020).

Neutrino fluxes Φ from each MESA calibrated solar model and Vinyoles et al. (2017) models are compared to the observations in Figure 9 and Table 3. Φ(pp), and Φ(pep) are well within $1\,\sigma$ of their inferred observational value. The fractional variation in $\delta\Phi$(pp), $\delta\Phi$(pep) $\propto -0.9,\ -1.4\,\delta T$ (Villante & Serenelli 2021) is a nearly linear relationship with the fractional variation in the temperature δT. Therefore, the variation of nearly $\sim 9\%$ in the observational value for Φ(pp) and Φ(pep) allows for a similar level of deviation in these nuclear reaction rates. However, these rates are constrained at the nearly $\sim 1\%$ level (Adelberger et al. 2011), suggesting the current neutrino flux statistics for Φ(pp) and Φ(pep) do not presently constrain the T of the solar core. Our results show similar Φ(pp) regardless of the adopted opacity table and slightly higher neutrino fluxes from Φ(pep) in the OPLIB-based models than the OP- and OPAL-based models. All solar models, regardless of the adopted opacity table, reliably predict the value of Φ(hep) to be roughly an order of magnitude lower than the currently measured upper limit.

The $\Phi(^7\text{Be})$ and $\Phi(^8\text{B})$ fluxes place the tightest constraints on the solar core T with $\delta\Phi(^7\text{Be})$, $\delta\Phi(^8\text{B}) \propto -11,\ -24\,\delta T$ (Villante & Serenelli 2021). The lower core T produced by the OPLIB-based solar models results in significantly lower $\Phi(^7\text{Be})$ and $\Phi(^8\text{B})$ versus the OP or OPAL models regardless of initial Z. Higher Z solar models systematically produce larger ^{7}Be and ^{8}B neutrino fluxes. The metallicity is most important in determining the CNO flux Φ(CNO), which appears to agree only with the latter metallicity GS98/MB22 models regardless of the chosen opacity table. OPLIB-based solar models show a slight decrease in Φ(CNO) resulting from their lower core T.

Despite many differences in model physics between our MESA models and the B16 standard solar models from Vinyoles et al. (2017), our neutrino flux results are in good agreement with theirs. Overall, OPLIB opacities produce sufficiently different neutrino flux and helioseismic quantities to warrant the reinvestigation of solar models with additional input physics such as rotation, accretion, and other mixing mechanisms which could alter the chemical stratification of these solar models (Guzik & Mussack 2010; Wood et al. 2018; Zhang et al. 2019; Kunitomo & Guillot 2021; Kunitomo et al. 2022). It is conceivable that the true solar abundances in the core are higher than in the envelope.

4. Conclusion

We presented highlights of a new set of 1194 Type-1 Rosseland mean opacity tables for four different metallicity mixtures. These new Los Alamos OPLIB radiative opacity tables are an order of magnitude larger in number than any previous opacity table release, and span regimes where previous opacity tables have not existed. For example, the new set of opacity tables expands the metallicity range to $Z = 10^{-6}$ to $Z = 0.2$, which allows improved accuracy of opacities at low and high metallicity. In addition, the table density in the metallicity range $Z = 10^{-4}$ to $Z = 0.1$ is enhanced to improve the accuracy of opacities drawn from interpolations across neighboring metallicities. Finally, there are new opacity tables for hydrogen mass fractions between $X = 0$ and $X = 0.1$ including $X = 10^{-2}$, 10^{-3}, 10^{-4}, 10^{-5}, and 10^{-6} that can improve stellar models of hydrogen deficient stars. This larger set of opacity tables results in a $\approx$2%–2.5% improvement across the X–Z plane. At $Z > 0.1$ the improvement can reach up to 50% in MESA. The largest improvement, up to $\approx$70, is observed between $3.8 \leqslant \log T \leqslant 4.8$ and $0 < X < 0.1$: the hydrogen-poor regime, which can be encountered in stellar models with effective gravitational settling. Differences between using the new 1194 OPLIB opacity tables and the 126 OPAL opacity tables range from $\approx$20% to 80% across individual chemical mixtures.

We implemented and verified these new OPLIB radiative opacity tables in MESA. We found that calibrated solar models produced with these new OPLIB tables agree broadly with previously published helioseismic and neutrino results found in the literature. In hotter and denser regimes, our calculated OPLIB opacity tables yield higher opacities than OP/OPAL. In colder models such as solar models, OPLIB opacity tables

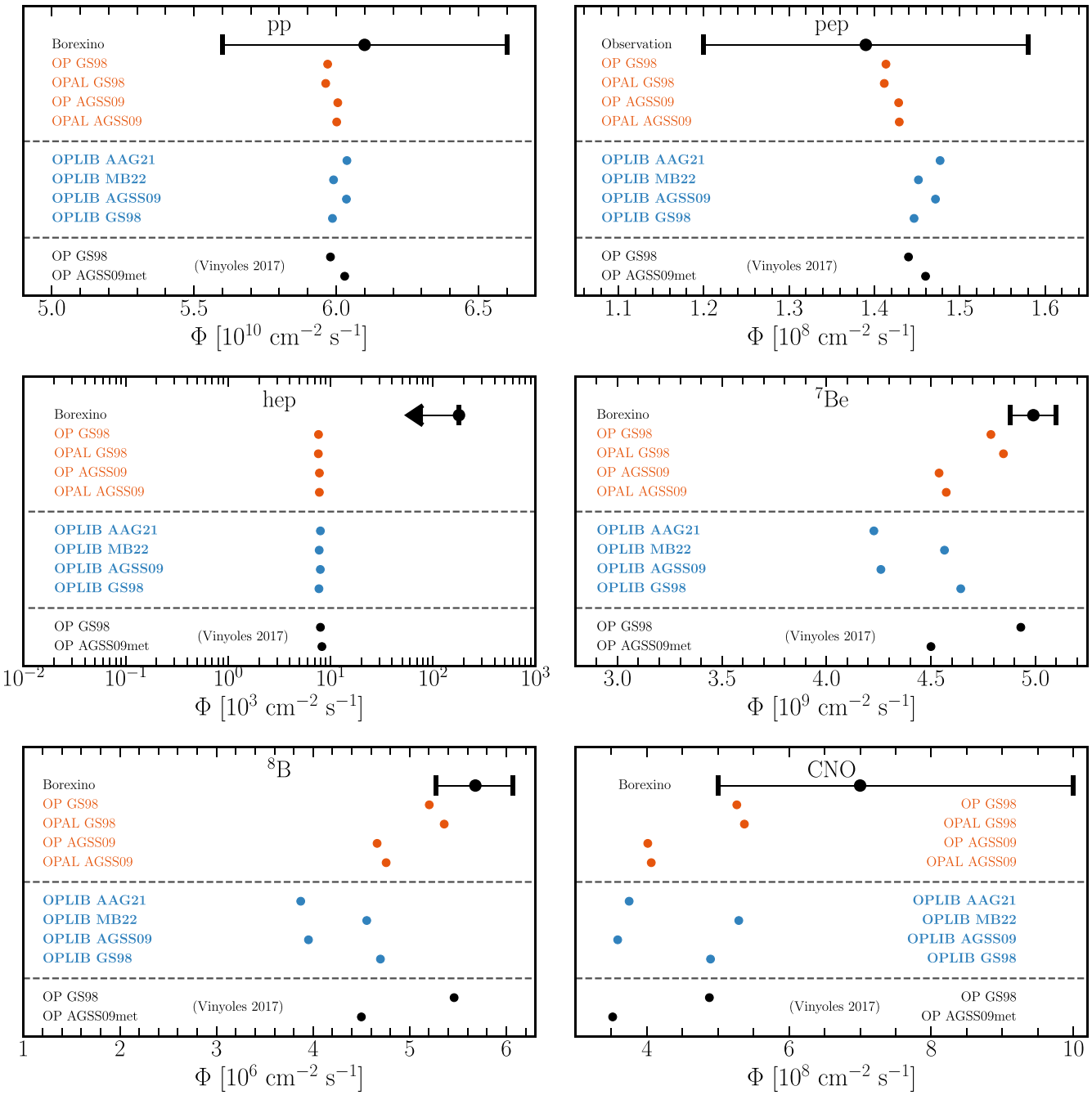

Figure 9. Neutrino fluxes and uncertainties compared to solar neutrino observations from the Borexino Collaboration (Bellini et al. 2011) as presented in Haxton et al. (2013), Villante et al. (2014), and Kumaran et al. (2021). Standard solar model results using previous opacity sets are shown in orange, results using the new 1194 OPLIB opacity tables are shown in blue, and results from Vinyoles et al. (2017) are shown in black. See Table 3 for the data behind this figure.

predict lower core opacities, lower core T, and higher core ρ than OP/OPAL. Overall, we find differences in the opacity table source (OP, OPAL, OPLIB) result in solar model opacity differences of ≈8% and ≈15% at the bottom and top of the solar convection zone, and up to ≈7% in the solar core. We find that standard solar models produced with the OPLIB opacities produce lower neutrino fluxes and markedly different helioseismology than OP/OPAL models. We also find that standard solar models computed with higher-metallicity mixtures (GS98 or MB22) are in better agreement with helioseismic and neutrino constraints than low-metallicity mixtures (AGSS09 or AAG21) regardless of the adopted opacity table. We find that the new OPLIB opacity tables do not solve the solar modeling problem when used in standard solar models. This suggests that physical mechanisms other than the atomic radiative opacity should be further investigated in order to solve the solar modeling problem (Guzik 2008; Serenelli et al. 2009; Guzik & Mussack 2010; Salmon et al. 2021; Eggenberger et al. 2022; Buldgen et al. 2023).

We also tested the opacity interpolation schemes adopted in MESA for interpolation across the X–Z plane. We find that linear interpolation systematically underpredicts the opacity by 3%–60% across metallicities and up to 10% in solar models, as compared to cubic interpolation. We find MESA solar models must adopt cubic interpolation in X–Z to produce helioseismic results consistent with other published works. We leave further

Table 3
Solar Neutrino Fluxes

Component	Φ_{pp}	Φ_{pep}	Φ_{hep}	Φ_{Be7}	Φ_{B8}	Φ_{CNO}
Observed	$6.1 \pm (0.5^{+0.3}_{-0.5})$	$1.39 \pm (0.19^{+0.08}_{-0.13})$	$\leqslant$180 (90% CL)	$4.99 \pm (0.11^{+0.06}_{-0.08})$	$5.68 \pm (^{+0.39}_{-0.41}\ ^{+0.03}_{-0.03})$	$7.0^{+3.0}_{-2.0}$
Currently in MESA						
OPAL_126 GS98	5.964	1.412	7.615	4.856	5.374	5.395
OPAL_126 AGSS09	6.003	1.430	7.794	4.573	4.754	4.060
OP_126 GS98	5.970	1.414	7.641	4.796	5.221	5.291
OP_126 AGSS09	6.007	1.429	7.803	4.540	4.662	4.012
This Work						
OPLIB_168 GS98	5.987	1.447	7.719	4.640	4.692	4.892
OPLIB_126 AGSS09	6.035	1.472	7.955	4.274	3.974	3.597
OPLIB_126 AAG21	6.038	1.477	7.976	4.227	3.872	3.751
OPLIB_126 MB22	5.991	1.452	7.762	4.562	4.551	5.288
OPLIB_1194 GS98	5.987	1.447	7.717	4.643	4.697	4.896
OPLIB_1194 AGSS09	6.036	1.472	7.961	4.260	3.952	3.590
OPLIB_1194 AAG21	6.039	1.476	7.980	4.217	3.857	3.748
OPLIB_1194 MB22	5.991	1.452	7.760	4.565	4.555	5.293
Vinyoles et al. (2017)						
OP_126 GS98	5.98	1.44	7.98	4.93	5.46	4.88
OP_126 AGSS09met	6.03	1.46	8.25	4.50	4.50	3.52

Note.
[a] Observations from the Borexino Collaboration (Bellini et al. 2011) as presented in Haxton et al. (2013), Villante et al. (2014), and Kumaran et al. (2021). Flux scales for Φ (in cm^{-2} s^{-1}) are: 10^{10} (pp); 10^{8} (pep); 10^{3} (hep); 10^{9} (Be); 10^{6} (B); 10^{8} (CNO).

exploration and improvements to MESA's opacity interpolation methods to future work.

The low-temperature opacity tables used in this article will be included in the forthcoming public release of MESA and can be directly downloaded from http://www.wichita.edu/academics/fairmount_las/physics/Research/opacity.php. The new Los Alamos OPLIB radiative opacity tables presented in this article will be available at http://aphysics2.lanl.gov/opacity/lanl and will also be included in a forthcoming public release of MESA. Users can also generate opacity tables for their own desired mixtures at http://aphysics2.lanl.gov/opacity/lanl. We encourage future stellar physics research to experiment with this expanded set of Type-1 Rosseland mean opacity tables.

Acknowledgments

We thank Luis Trivino at Los Alamos National Laboratory for his pivotal help in providing computing resources for this project. We also thank Jason Ferguson and David Alexander for providing the low-temperature opacity tables for the MB22 and AAG21 mixtures. This research was partially supported by the National Science Foundation under grant 2154339 and by the U.S. Department of Energy through the Los Alamos National Laboratory. Los Alamos National Laboratory is operated by Triad National Security, LLC, for the National Nuclear Security Administration of the U.S. Department of Energy (Contract No. 89233218CNA000001). This research made extensive use of the SAO/NASA Astrophysics Data System (ADS).

Software: MESA (Paxton et al. 2011, 2013, 2015, 2018, 2019; Jermyn et al. 2023, https://docs.mesastar.org), MESASDK 20190830 (Townsend 2019a, 2019b), matplotlib (Hunter 2007), Scipy (Virtanen et al. 2020), and NumPy (van der Walt et al. 2011).

Appendix

Appendices A, B, and C detail the implementation and verification of the new OPLIB tables in MESA. Appendix A discusses the use of bicubic splines on the raw OPLIB tables, Appendix B compares linear and cubic interpolation of opacities across X–Z in MESA, and Appendix C compares the helioseismic differences between MESA solar models calculated with linear and cubic interpolation of the opacities across the X–Z plane.

Appendix A
Bicubic Splines of OPLIB Tables in MESA

To ensure smooth opacity derivatives, OPAL and OP opacity tables have historically been run through smoothing and spline-fitting routines, see Seaton (1993). We generate bicubic spline versions of the raw OPLIB tables using a Python Scipy routine. We interpolate the original 74 $\log(T/\mathrm{K})\times 39$ $\log(R)$ point OPLIB tables spanning $3.764 \leqslant \log(T/\mathrm{K}) \leqslant 9.065$ and $-8.0 \leqslant \log(R) \leqslant 1.5$ into evenly spaced 213 $\log(T/\mathrm{K})\times 39$ $\log(R)$ opacity tables spanning $3.75 \leqslant \log(T/\mathrm{K}) \leqslant 9.05$ with $\Delta T = 0.025$, and identical spacing in $\log(R)$. Figure A1 shows the raw OPLIB and bicubic spline fits for an $X = 0.7$, $Z = 0.02$ mixture along constant $\log(R)$ and their respective normalized differences. Overall, the bicubic spline smoothing of the OPLIB tables results in $\lesssim 0.5\%$ changes to the overall opacity, except for $\log(T/\mathrm{K}) \lesssim 4$, where the OPLIB tables are less smooth.

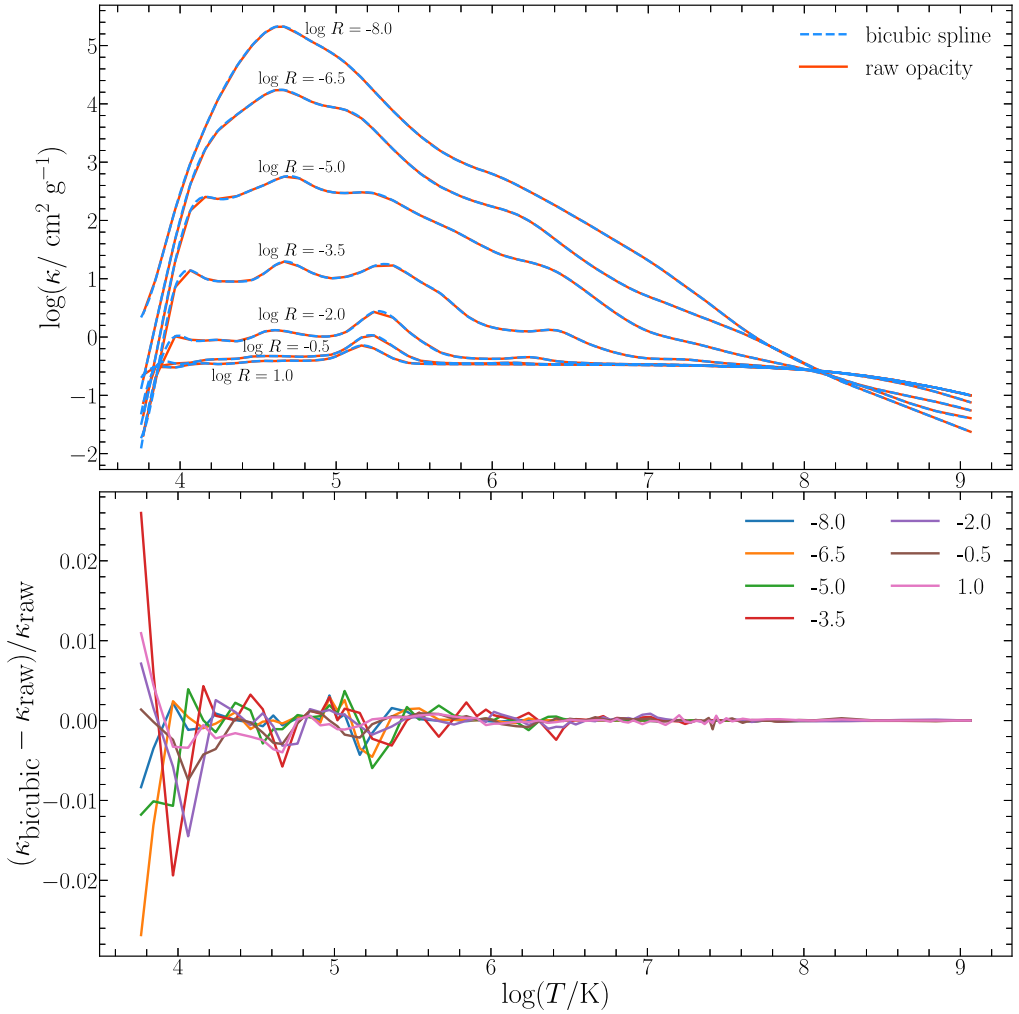

Figure A1. Top panel: opacity vs. temperature for different log(R) from a GS98 OPLIB opacity table at $X = 0.7$, $Z = 0.02$ for different log(R). The bicubic spline interpolation is overlaid as a dashed curve. Bottom panel: normalized difference between the bicubic spline interpolations and the raw OPLIB tables for various values of log(R).

Appendix B
MESA Linear versus Cubic Interpolation in X–Z

The default interpolation scheme across the X–Z plane in MESA uses linear interpolation:

```
cubic_interpolation_in_X=.false.
cubic_interpolation_in_Z=.false.
```

Figure B1 shows the normalized opacity differences between the cubic interpolated OPLIB 126 table set (denoted κ_{cubic}) and the linear interpolated OPLIB 126 table set (denoted κ_{linear}) for six mixtures in the $\rho - T$ plane. The six mixtures are chosen to lie between the available tables in the X–Z plane. Overall we find linear interpolation systematically underpredicts the opacity by up to 60% depending on the metallicity.

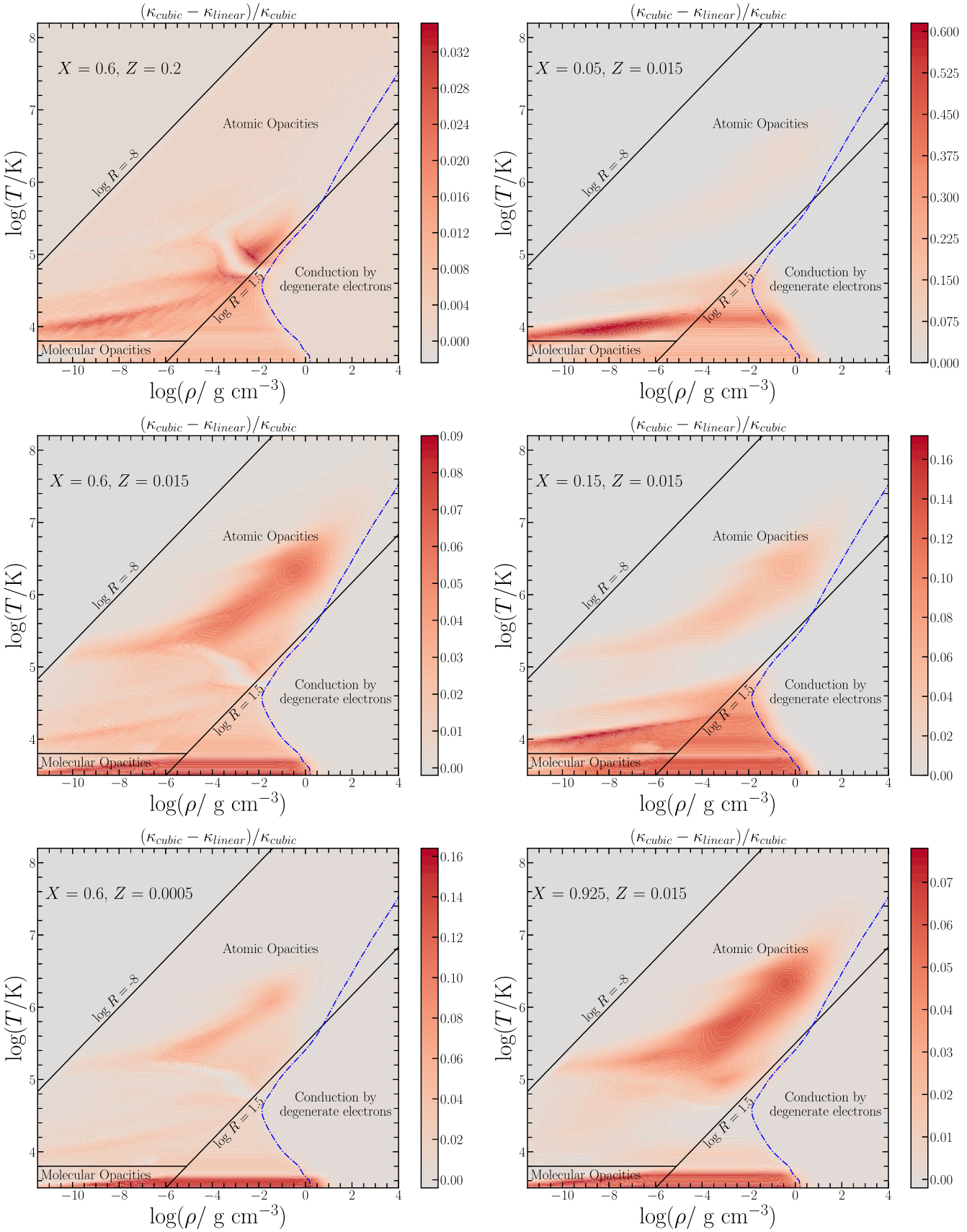

Figure B1. Relative differences between the 126 OPLIB opacity tables with cubic vs. linear interpolation using Grevesse & Sauval (1998) abundances, generated from MESA's kap module, for six mixtures. The left column shows mixtures with $X = 0.6$ and varying Z, and the right column shows mixtures with $Z = 0.015$ and varying X. The OPLIB $\log(R) = -8$, 1.5 table boundaries are marked with a solid black line. The approximate location of the Z-dependent transition to an electron-conduction-dominated opacity is marked with a dotted–dashed blue curve.

Appendix C
MESA Solar Models with Linear versus Cubic Interpolation in *X*–*Z*

We briefly illustrate the helioseismic differences arising from using linear and cubic interpolation in the *X*–*Z* plane for standard solar models calibrated with the OP/OPAL opacity tables and GS98/AGSS09 abundances included in MESA. Figure C1 shows the relative sound speed and density profiles of solar models calculated with linear and cubic interpolation. The agreement with helioseismic data is systemically worse for solar models that use linear interpolation in *X*–*Z*. The sound speed and density profiles from models that use cubic interpolation are in better agreement with solar model results found in the literature (e.g., Vinyoles et al. 2017; Magg et al. 2022) than those run with linear interpolation.

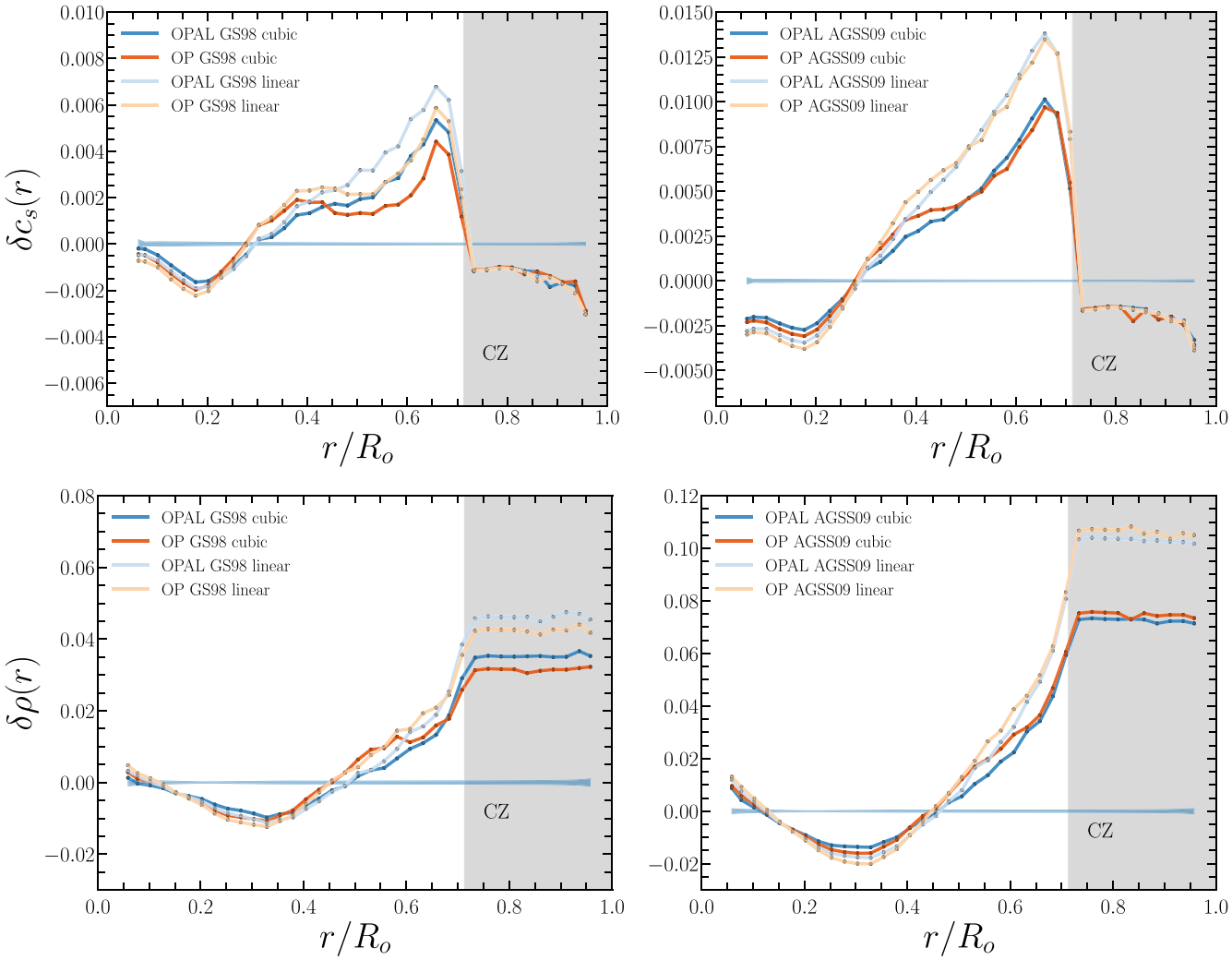

Figure C1. Fractional sound speed and density differences, $\delta c_s = (c_{\rm obs}$ - $c_s(r))/c_s(r)$ and $\delta\rho = (\rho_{\rm obs}$ - $\rho(r))/\rho(r)$, between the values predicted by a calibrated MESA standard solar model, $c_s(r)$ and $\rho(r)$, and the $c_{\rm obs}$ and $\rho_{\rm obs}$ values inferred from helioseismic data (Basu et al. 2009). The 1σ observational uncertainties are shown as the blue bands at ordinates of zero. Black circles mark locations where δc_s and $\delta\rho$ are evaluated. Gray bands show the convective regions, labeled CZ.

ORCID iDs

Ebraheem Farag https://orcid.org/0000-0002-5794-4286
Christopher J. Fontes https://orcid.org/0000-0003-1087-2964
F. X. Timmes https://orcid.org/0000-0002-0474-159X
Earl P. Bellinger https://orcid.org/0000-0003-4456-4863
Joyce A. Guzik https://orcid.org/0000-0003-1291-1533
Evan B. Bauer https://orcid.org/0000-0002-4791-6724
Suzannah R. Wood https://orcid.org/0000-0002-7208-7681
Katie Mussack https://orcid.org/0000-0002-5539-9034
Peter Hakel https://orcid.org/0000-0002-7936-4231
James Colgan https://orcid.org/0000-0003-1045-3858
David P. Kilcrease https://orcid.org/0000-0002-2319-5934
Manolo E. Sherrill https://orcid.org/0000-0002-0312-7694
Tryston C. Raecke https://orcid.org/0009-0002-2268-7352
Morgan T. Chidester https://orcid.org/0000-0002-5107-8639

References

Abdallah, J., Kilcrease, D. P., Magee, N. H., et al. 2007, HEDP, 3, 309
Adelberger, E. G., García, A., Robertson, R. G. H., et al. 2011, RvMP, 83, 195
Aerts, C., Christensen-Dalsgaard, J., & Kurtz, D. W. 2010, Asteroseismology (Berlin: Springer)
Alastuey, A., & Jancovici, B. 1978, ApJ, 226, 1034
Angulo, C., Arnould, M., Rayet, M., et al. 1999, NuPhA, 656, 3
Antia, H. M., & Basu, S. 1994a, ApJ, 426, 801
Antia, H. M., & Basu, S. 1994b, A&AS, 107, 421
Asplund, M., Amarsi, A. M., & Grevesse, N. 2021, A&A, 653, A141
Asplund, M., Grevesse, N., Sauval, A. J., & Scott, P. 2009, ARA&A, 47, 481
Badnell, N. R., Bautista, M. A., Butler, K., et al. 2005, MNRAS, 360, 458
Bahcall, J. N., & Pinsonneault, M. H. 2004, PhRvL, 92, 121301
Bahcall, J. N., Serenelli, A. M., & Basu, S. 2006, ApJS, 165, 400
Bahcall, J. N., & Ulmer, A. 1996, PhRvD, 53, 4202
Bahcall, J. N., & Ulrich, R. K. 1988, RvMP, 60, 297
Ball, W. H. 2021, RNAAS, 5, 7
Balona, L. A. 2018, FrASS, 5, 43
Basu, S. 2016, LRSP, 13, 2
Basu, S., & Antia, H. M. 1995, MNRAS, 276, 1402
Basu, S., & Antia, H. M. 1997, MNRAS, 287, 189
Basu, S., & Antia, H. M. 2004, ApJL, 606, L85
Basu, S., & Antia, H. M. 2008, PhR, 457, 217
Basu, S., Chaplin, W. J., Elsworth, Y., New, R., & Serenelli, A. M. 2009, ApJ, 699, 1403
Basu, S., Mazumdar, A., Antia, H. M., & Demarque, P. 2004, MNRAS, 350, 277
Bellinger, E. P., & Christensen-Dalsgaard, J. 2022, MNRAS, 517, 5281
Bellini, G., Benziger, J., Bick, D., et al. 2011, PhRvL, 107, 141302
Bigot, L., & Dziembowski, W. A. 2002, A&A, 391, 235
Blancard, C., Cossé, P., & Faussurier, G. 2012, ApJ, 745, 10
Blouin, S., Dufour, P., Thibeault, C., & Allard, N. F. 2019, ApJ, 878, 63
Blouin, S., Shaffer, N. R., Saumon, D., & Starrett, C. E. 2020, ApJ, 899, 46
Bouvier, A., & Wadhwa, M. 2010, NatGe, 3, 637
Bowman, D. M., & Kurtz, D. W. 2018, MNRAS, 476, 3169
Brown, T. M., & Morrow, C. A. 1987, in Proc. 8th National Solar Observatory Summer Symp. 137, The Internal Solar Angular Velocity, ed. B. R. Durney & S. Sofia (Reidel: Dordrecht), 7
Buldgen, G., Eggenberger, P., Baturin, V. A., et al. 2020, A&A, 642, A36
Buldgen, G., Eggenberger, P., Noels, A., et al. 2023, A&A, 669, L9
Buldgen, G., Noels, A., Baturin, V. A., et al. 2024, A&A, 681, A57
Buldgen, G., Salmon, S., & Noels, A. 2019, FrASS, 6, 42
Carson, T. R. 1976, ARA&A, 14, 95
Carson, T. R., Mayers, D. F., & Stibbs, D. W. N. 1968, MNRAS, 140, 483
Cassisi, S., Potekhin, A. Y., Pietrinferni, A., Catelan, M., & Salaris, M. 2007, ApJ, 661, 1094
Chandrasekhar, S. 1944, ApJ, 100, 176
Chandrasekhar, S., & Breen, F. H. 1946, ApJ, 104, 430
Christensen-Dalsgaard, J. 2021, LRSP, 18, 2
Christensen-Dalsgaard, J., Duvall, T. L. J., Gough, D. O., Harvey, J. W., & Rhodes, E. J. J. 1985, Natur, 315, 378
Christensen-Dalsgaard, J., Gough, D. O., & Thompson, M. J. 1991, ApJ, 378, 413
Christy, R. F. 1966, ApJ, 144, 108
Chugunov, A. I., Dewitt, H. E., & Yakovlev, D. G. 2007, PhRvD, 76, 025028
Colgan, J., Kilcrease, D. P., Magee, N. H., et al. 2016, ApJ, 817, 116
Córsico, A. H., Althaus, L. G., Miller Bertolami, M. M., & Kepler, S. O. 2019, A&ARv, 27, 7
Cowan, R. D. 1981, The Theory of Atomic Structure and Spectra (Los Alamos Series in Basic and Applied Sciences) (Berkeley, CA: Univ. California Press)
Cox, A. N. 1965, in Stellar Structure—Stars and Stellar Systems, ed. L. H. Aller & D. B. McLaughlin (Chicago, IL: Univ. Chicago Press), 195
Cox, A. N., & Stewart, J. N. 1962, AJ, 67, 113
Cox, A. N., & Stewart, J. N. 1970a, ApJS, 19, 243
Cox, A. N., & Stewart, J. N. 1970b, ApJS, 19, 261
Cox, A. N., & Tabor, J. E. 1976, ApJS, 31, 271
Cox, J. P. 1980, Theory of Stellar Pulsation, Princeton Series in Astrophysics (Princeton, NJ: Princeton Univ. Press)
Cox, J. P., & Giuli, R. T. 1968, Principles of Stellar Structure (New York: Gordon & Breach)
Cugier, H. 2012, A&A, 547, A42
Cyburt, R. H., Amthor, A. M., Ferguson, R., et al. 2010, ApJS, 189, 240
Das, S., Kanbur, S. M., Bellinger, E. P., et al. 2020, MNRAS, 493, 29
Daszyńska-Daszkiewicz, J., Pamyatnykh, A. A., Walczak, P., et al. 2017, MNRAS, 466, 2284
Daszyńska-Daszkiewicz, J., & Walczak, P. 2009, MNRAS, 398, 1961
Daszyńska-Daszkiewicz, J., & Walczak, P. 2010, MNRAS, 403, 496
Daszyńska-Daszkiewicz, J., Walczak, P., Pamyatnykh, A., Szewczuk, W., & Niewiadomski, W. 2023, ApJL, 942, L38
Degl'Innoccenti, S., Dziembowski, W. A., Fiorentini, G., & Ricci, B. 1997, APh, 7, 77
Dewitt, H. E., Graboske, H. C., & Cooper, M. S. 1973, ApJ, 181, 439
Doughty, N. A., & Fraser, P. A. 1966, MNRAS, 132, 267
Dziembowski, W. A., Pamiatnykh, A. A., & Sienkiewicz, R. 1991, MNRAS, 249, 602
Eddington, A. S. 1926, The Internal Constitution of the Stars (Cambridge: Cambridge Univ. Press)
Eggenberger, P., Buldgen, G., Salmon, S. J. A. J., et al. 2022, NatAs, 6, 788
Fadeyev, Y. A. 2022, MNRAS, 514, 5996
Farag, E., Timmes, F. X., Chidester, M. T., Anandagoda, S., & Hartmann, D. H. 2024, ApJS, 270, 5
Farag, E., Timmes, F. X., Taylor, M., Patton, K. M., & Farmer, R. 2020, ApJ, 893, 133
Farmer, R., Fields, C. E., Petermann, I., et al. 2016, ApJS, 227, 22
Ferguson, J. W., Alexander, D. R., Allard, F., et al. 2005, ApJ, 623, 585
Flörs, A., Silva, R. F., Deprince, J., et al. 2023, MNRAS, 524, 3083
Fontes, C. J., Fryer, C. L., Wollaeger, R. T., Mumpower, M. R., & Sprouse, T. M. 2023, MNRAS, 519, 2862
Fontes, C. J., Zhang, H. L., Abdallah, J. J., et al. 2015, JPhB, 48, 144014
Fox, M. W., & Wood, P. R. 1982, ApJ, 259, 198
Freedman, R. S., Marley, M. S., & Lodders, K. 2008, ApJS, 174, 504
Fuller, G. M., Fowler, W. A., & Newman, M. J. 1985, ApJ, 293, 1
Gaunt, J. A. 1930, RSPTA, 229, 163
Gough, D. O. 1990, in Proc. Oji International Seminar 367, Progress of Seismology of the Sun and Stars, ed. Y. Osaki & H. Shibahashi (Berlin: Springer), 283
Graboske, H. C., Dewitt, H. E., Grossman, A. S., & Cooper, M. S. 1973, ApJ, 181, 457
Grevesse, N., & Sauval, A. J. 1998, SSRv, 85, 161
Guzik, J., Fontes, C., & Fryer, C. 2018, Atoms, 6, 31
Guzik, J. A. 2008, MmSAI, 79, 481
Guzik, J. A. 2021, FrASS, 8, 55
Guzik, J. A., Fontes, C. J., Walczak, P., et al. 2016, IAUFM, 29B, 532
Guzik, J. A., & Mussack, K. 2010, ApJ, 713, 1108
Hakel, P., & Kilcrease, D. P. 2004, in AIP Conf. Ser. 730, Atomic Processes in Plasmas: 14th APS Topical Conf. on Atomic Processes in Plasmas, ed. J. S. Cohen, D. P. Kilcrease, & S. Mazevet (Melville, NY: AIP), 190
Hakel, P., Sherrill, M. E., Mazevet, S., et al. 2006, JQSRT, 99, 265
Hansen, C. J., Kawaler, S. D., & Trimble, V. 2004, Stellar Interiors: Physical Principles, Structure, and Evolution (New York: Springer)
Haxton, W. C., Hamish Robertson, R. G., & Serenelli, A. M. 2013, ARA&A, 51, 21
Haxton, W. C., & Serenelli, A. M. 2008, ApJ, 687, 678
Heger, A., Jeannin, L., Langer, N., & Baraffe, I. 1997, A&A, 327, 224
Holdsworth, D. L., Cunha, M. S., Kurtz, D. W., et al. 2021, MNRAS, 506, 1073
Hübner, W., Merts, A., Magee, N., & argo, M. 1977, Astrophysical Opacity Library, Tech. Report LA-6760-M, Los Alamos National Laboratory

Huebner, W. F., & Barfield, W. D. 2014, Opacity, Vol. 402 (New York: Springer)
Hui-Bon-Hoa, A. 2021, A&A, 646, L6
Hunter, J. D. 2007, CSE, 9, 90
Iben, I., Jr 1975, ApJ, 196, 525
Iglesias, C. A., & Rogers, F. J. 1993, ApJ, 412, 752
Iglesias, C. A., & Rogers, F. J. 1996, ApJ, 464, 943
Iglesias, C. A., Rogers, F. J., & Saumon, D. 2002, ApJL, 569, L111
Iglesias, C. A., & Sonnad, V. 2012, HEDP, 8, 154
Ignjatović, L. M., Mihajlov, A. A., Sakan, N. M., Dimitrijević, M. S., & Metropoulos, A. 2009, MNRAS, 396, 2201
Itoh, N., Totsuji, H., Ichimaru, S., & Dewitt, H. E. 1979, ApJ, 234, 1079
Jermyn, A. S., Bauer, E. B., Schwab, J., et al. 2023, ApJS, 265, 15
Jin, J.-h. 1982, ChA&A, 6, 20
John, T. L. 1994, MNRAS, 269, 871
Kilcrease, D. P., Colgan, J., Hakel, P., Fontes, C. J., & Sherrill, M. E. 2015, HEDP, 16, 36
Kippenhahn, R., & Weigert, A. 1990, Stellar Structure and Evolution (Berlin: Springer)
Kippenhahn, R., Weigert, A., & Weiss, A. 2012, Stellar Structure and Evolution (Berlin: Springer)
Kosovichev, A. G. 1993, MNRAS, 265, 1053
Kowalski, P. M. 2014, A&A, 566, L8
Kramers, H. 1923, PMag, 46, 836
Krief, M., Feigel, A., & Gazit, D. 2016, ApJ, 824, 98
Kumaran, S., Ludhova, L., Penek, Ö., & Settanta, G. 2021, Univ, 7, 231
Kunitomo, M., & Guillot, T. 2021, A&A, 655, A51
Kunitomo, M., Guillot, T., & Buldgen, G. 2022, A&A, 667, L2
Kurtz, D. W. 1982, MNRAS, 200, 807
Kurtz, D. W. 2022, ARA&A, 60, 31
Landolt, A. U. 1968, ApJ, 153, 151
Langanke, K., & Martínez-Pinedo, G. 2000, NuPhA, 673, 481
Le Pennec, M., Turck-Chièze, S., Salmon, S., et al. 2015, ApJL, 813, L42
Magee, N. H., Abdallah, J., Colgan, J., et al. 2004, in AIP Conf. Ser. 730, Atomic Processes in Plasmas: 14th APS Topical Conference on Atomic Processes in Plasmas, ed. J. S. Cohen, D. P. Kilcrease, & S. Mazevet (Melville, NY: AIP), 168
Magee, N. H., Abdallah, J. J., Clark, R. E. H., et al. 1995, in ASP Conf. Ser. 78, Astrophysical Applications of Powerful New Databases, ed. S. J. Adelman & W. L. Wiese (San Francisco, CA: ASP), 51
Magg, E., Bergemann, M., Serenelli, A., et al. 2022, A&A, 661, A140
Marigo, P., & Aringer, B. 2009, A&A, 508, 1539
Mayer, H. 1947, Methods of Opacity Calculations, Tech. Report LA-647, Los Alamos National Laboratory
Mazumdar, A., Monteiro, M. J. P. F. G., Ballot, J., et al. 2014, ApJ, 782, 18
Meyer-Hofmeister, E. 1982, in Landolt-Bornstein: Group 6: Astronomy, Vol. 2
Meyerott, R., & Moszkowski, S. 1951, Photon Absorption Coefficients Of Light Elements And Mixtures, Tech. Report ANL-4594, Argonne National Laboratory
Mihalas, D. 1978, Stellar Atmospheres (San Francisco, CA: W.H. Freeman)
Mihalas, D., & Mihalas, B. W. 1984, Foundations of Radiation Hydrodynamics (New York: Oxford Univ. Press)
Mondet, G., Blancard, C., Cossé, P., & Faussurier, G. 2015, ApJS, 220, 2
Moszkowski, S., & Meyerott, R. 1951, Opacity Calculations for Light Elements and Mixtures, Tech. Report ANL-4743, Argonne National Laboratory
Murphy, S. J., Bedding, T. R., Gautam, A., & Joyce, M. 2023, MNRAS, 526, 3779
Nahar, S. N., Zhao, L., Eissner, W., & Pradhan, A. K. 2024, JPhB, 57, 125002
Neuforge-Verheecke, C., Goriely, S., Guzik, J. A., Swenson, F. J., & Bradley, P. A. 2001a, ApJ, 550, 493
Neuforge-Verheecke, C., Guzik, J. A., Keady, J. J., et al. 2001b, ApJ, 561, 450
Ngeow, C.-C., Bhardwaj, A., Dekany, R., et al. 2022, AJ, 163, 239
Oda, T., Hino, M., Muto, K., Takahara, M., & Sato, K. 1994, ADNDT, 56, 231
Ohmura, T. 1964, ApJ, 140, 282
Ohmura, T., & Ohmura, H. 1960, ApJ, 131, 8
Pain, J.-C., & Gilleron, F. 2015, HEDP, 15, 30
Pain, J.-C., & Gilleron, F. 2019, arXiv:1901.08959
Pain, J.-C., Gilleron, F., & Comet, M. 2017, Atoms, 5, 22
Paxton, B., Bildsten, L., Dotter, A., et al. 2011, ApJS, 192, 3
Paxton, B., Cantiello, M., Arras, P., et al. 2013, ApJS, 208, 4
Paxton, B., Marchant, P., Schwab, J., et al. 2015, ApJS, 220, 15
Paxton, B., Schwab, J., Bauer, E. B., et al. 2018, ApJS, 234, 34
Paxton, B., Smolec, R., Schwab, J., et al. 2019, ApJS, 243, 10
Poutanen, J. 2017, ApJ, 835, 119
Pradhan, A. K. 2024, JPhB, 57, 125003
Pradhan, A. K., Nahar, S. N., & Eissner, W. 2024, JPhB, 57, 125001
Prša, A., Harmanec, P., Torres, G., et al. 2016, AJ, 152, 41
Raecke, T. C. 2022, Application of New Los Alamos OPLIB Opacities in Solar Modeling Using the Mesa Code LA-UR-22-27983, Los Alamos National Laboratory
Richard, O., Dziembowski, W. A., Sienkiewicz, R., & Goode, P. R. 1998, A&A, 338, 756
Rogers, F. J., & Iglesias, C. A. 1992, ApJS, 79, 507
Rohrmann, R. D. 2018, MNRAS, 473, 457
Saio, H. 1993, Ap&SS, 210, 61
Salmon, S. J. A. J., Buldgen, G., Noels, A., et al. 2021, A&A, 651, A106
Saumon, D., Blouin, S., & Tremblay, P.-E. 2022, PhR, 988, 1
Saunders, D. P., Ong, J. M. J., & Basu, S. 2023, ApJ, 947, 22
Schwarzschild, M. 1958, Structure and Evolution of the Stars (Princeton, NJ: Princeton Univ. Press)
Seaton, M. J. 1987, JPhB, 20, 6363
Seaton, M. J. 1993, MNRAS, 265, L25
Seaton, M. J. 2005, MNRAS, 362, L1
Seaton, M. J., & Badnell, N. R. 2004, MNRAS, 354, 457
Seaton, M. J., Yan, Y., Mihalas, D., & Pradhan, A. K. 1994, MNRAS, 266, 805
Serenelli, A. M., Basu, S., Ferguson, J. W., & Asplund, M. 2009, ApJL, 705, L123
Shi, X.-d., Qian, S.-b., Zhu, L.-y., et al. 2023, ApJS, 265, 33
Shibahashi, H., & Takata, M. 1993, PASJ, 45, 617
Simonucci, S., Taioli, S., Palmerini, S., & Busso, M. 2013, ApJ, 764, 118
Smith, H. A. 2004, RR Lyrae Stars (Cambridge: Cambridge Univ. Press)
Somerville, W. B. 1965, ApJ, 141, 811
Stellingwerf, R. F. 1975a, ApJ, 195, 441
Stellingwerf, R. F. 1975b, ApJ, 199, 705
Stonehill, L. C., Formaggio, J. A., & Robertson, R. G. 2004, PhRvC, 69, 015801
Thompson, M. J., Toomre, J., Anderson, E. R., et al. 1996, Sci, 272, 1300
Townsend, R. H. D. 2005, MNRAS, 364, 573
Townsend, R. H. D. 2019a, MESA SDK for Linux, 20190503, Zenodo, doi:10.5281/zenodo.2669541
Townsend, R. H. D. 2019b, MESA SDK for Mac OS, 20190503, Zenodo, doi:10.5281/zenodo.2669543
Trampedach, R., Stein, R. F., Christensen-Dalsgaard, J., Nordlund, Å., & Asplund, M. 2014, MNRAS, 442, 805
Turck-Chièze, S., Couvidat, S., Piau, L., et al. 2004, PhRvL, 93, 211102
van der Walt, S., Colbert, S. C., & Varoquaux, G. 2011, CSE, 13, 22
Vardya, M. S. 1964, ApJS, 8, 277
Verma, K., Raodeo, K., Antia, H. M., et al. 2017, ApJ, 837, 47
Verma, K., Raodeo, K., Basu, S., et al. 2019, MNRAS, 483, 4678
Villante, F. L., & Serenelli, A. 2021, FrASS, 7, 112
Villante, F. L., Serenelli, A. M., Delahaye, F., & Pinsonneault, M. H. 2014, ApJ, 787, 13
Vinyoles, N., Serenelli, A. M., Villante, F. L., et al. 2017, ApJ, 835, 202
Virtanen, P., Gommers, R., Oliphant, T. E., et al. 2020, NatMe, 17, 261
Vissani, F. 2019, in Proc. 5th Int. Solar Neutrino Conf., Solar Neutrinos, ed. M. Meyer et al. (Singapore: World Scientific), 121
Vitense, E. 1951, ZAp, 28, 81
Vorontsov, S. V., Baturin, V. A., & Pamiatnykh, A. A. 1991, Natur, 349, 49
Walczak, P., Fontes, C. J., Colgan, J., Kilcrease, D. P., & Guzik, J. A. 2015, A&A, 580, L9
Weiss, A., Keady, J. J., & Magee, N. H. J. 1990, ADNDT, 45, 209
Weiss, A., & Schlattl, H. 2008, Ap&SS, 316, 99
Wildt, R. 1939, ApJ, 90, 611
Wolf, W. M., Schwab, J., Farmer, R., & Bauer, E. B. 2023, ApJS, 269, 50
Wood, S. R., Mussack, K., & Guzik, J. A. 2018, SoPh, 293, 111
Xu, Y., Takahashi, K., Goriely, S., et al. 2013, NuPhA, 918, 61
Yoon, S.-C., & Cantiello, M. 2010, ApJL, 717, L62
Zhang, Q.-S., Li, Y., & Christensen-Dalsgaard, J. 2019, ApJ, 881, 103
Zhao, L., Nahar, S. N., Eissner, W., & Pradhan, A. K. 2024, JPhB, 57, 125004